HHS Public Access

Author manuscript

Nat Cancer. Author manuscript; available in PMC 2022 September 13.

Published in final edited form as:

Nat Cancer. 2022 January ; 3(1): 25–42. doi:10.1038/s43018-021-00297-3.

Astrocytic laminin-211 drives disseminated breast tumor cell dormancy in brain

Jinxiang Dai[1,§], **Patrick J. Cimino**[2,*], **Kenneth H. Gouin III**[3,*], **Candice A. Grzelak**[1], **Alexander Barrett**[4], **Andrea R. Lim**[1,5], **Annalyssa Long**[1], **Stephanie Weaver**[6], **Lindsey T. Saldin**[7], **Aiyedun Uzamere**[1], **Vera Schulte**[1], **Nigel Clegg**[1], **Laura Pisarsky**[1], **David Lyden**[8], **Mina J. Bissell**[9], **Simon Knott**[3], **Alana L. Welm**[10], **Jason H. Bielas**[1,2,11], **Kirk C. Hansen**[4], **Frank Winkler**[12], **Eric C. Holland**[11], **Cyrus M. Ghajar**[1,11,§]

[1]Public Health Sciences Division/Translational Research Program, Fred Hutchinson Cancer Research Center, Seattle, WA (USA)

[2]Department of Laboratory Medicine and Pathology, University of Washington, Seattle, WA (USA)

[3]Department of Biomedical Sciences; Applied Genomics, Computation and Translational Core, Cedars-Sinai Medical Center, Los Angeles, CA (USA)

[4]Department of Biochemistry and Molecular Genetics, University of Colorado Anschutz Medical Campus, Aurora, CO (USA)

[5]Graduate Program in Molecular and Cellular Biology, University of Washington, Seattle, WA (USA)

[6]Experimental Histopathology Core, Fred Hutchinson Cancer Research Center, Seattle, WA (USA)

[7]Department of Surgery, University of Pittsburgh, Pittsburgh, PA (USA)

[§]To whom correspondence should be addressed: Cyrus M. Ghajar, PhD, Public Health Sciences Division/Translational Research Program, Fred Hutchinson Cancer Research Center, 1100 Fairview Avenue N., M5-A864, Seattle, WA 98109 (USA), cghajar@fredhutch.org, P. 206.667.7080, F. 206.667.2537, Jinxiang Dai, PhD, Public Health Sciences Division/Translational Research Program, Fred Hutchinson Cancer Research Center, 1100 Fairview Avenue N., M5-A864, Seattle, WA 98109 (USA), jdai@fredhutch.org, P. 206.667.7082, F. 206.667.2537.

[*]These authors contributed equally.

Author Contributions Statement.

JD made fundamental intellectual contributions, performed experiments, and analyzed and interpreted data. PJC, ALW, SW and AU were instrumental to the acquisition and analysis of human tissue. CAG, ARL, SW, AU, LTS, LP and VS performed experiments and/or analyzed data. ARL helped with scientific illustration. AB and KCH conducted ECM-targeted mass spectrometry, and analyzed and interpreted the resulting data. JHB helped with design of the single cell RNA sequencing experiment; AL and NC conducted single cell RNA sequencing library preparation; KG and SK analyzed and interpreted the resulting data. MJB, DCL, FW and ECH provided key scientific insight. FW provided instruction for intravital imaging experiments. CMG conceived of the study, conducted experiments, and analyzed and interpreted data. CMG and JD wrote the manuscript. All authors read and provided feedback on the manuscript.

Peer Review Information:

Nature Cancer thanks Christoph Klein and the other, anonymous, reviewer(s) for their contribution to the peer review of this work.

Competing Interests Statement.

The authors declare no competing interests.

[8]Children's Cancer and Blood Foundation Laboratories, Departments of Pediatrics, and Cell and Developmental Biology, Drukier Institute for Children's Health, Meyer Cancer Center, Weill Cornell Medicine, New York, NY, (USA)

[9]Biological Systems and Engineering Division, Lawrence Berkeley National Laboratory, Berkeley, CA (USA)

[10]Department of Oncological Sciences, Huntsman Cancer Institute, University of Utah, Salt Lake City, UT (USA)

[11]Human Biology Division, Fred Hutchinson Cancer Research Center, Seattle, WA (USA)

[12]Neurology Clinic and National Center for Tumour Diseases, University Hospital Heidelberg, DKTK & Clinical Cooperation Unit Neurooncology, German Cancer Research Center, Heidelberg (Germany).

Abstract

Although dormancy is thought to play a key role in the metastasis of breast tumor cells to the brain, our knowledge of the molecular mechanisms regulating disseminated tumour cell (DTC) dormancy in this organ is limited. Here, using serial intravital imaging of dormant and metastatic triple-negative breast cancer lines, we identify escape from the single-cell or micro-metastatic state as the rate limiting step towards brain metastasis. We show that every DTC occupies a vascular niche, with quiescent DTCs residing on astrocyte endfeet. At these sites, astrocyte-deposited laminin-211 drives DTC quiescence by inducing the dystroglycan receptor to associate with yes-associated protein (YAP), thereby sequestering it from the nucleus and preventing its pro-metastatic functions. These findings identify a brain-specific mechanism of DTC dormancy and highlight the need for a more thorough understanding of tumor dormancy to develop therapeutic approaches that prevent brain metastasis.

Editor summary:

Ghajar and colleagues report that astrocyte-deposited laminin-211 promotes the quiescence of disseminated tumor cells in the brain, in a manner dependent on the cytoplasmic sequestration of YAP by dystroglycan.

Brain metastases are often difficult to treat and as a result, fatal[1]. This is due to a number of obstacles such as inability to deliver effective drug doses through the blood-brain barrier (**BBB**)[1], microenvironment-mediated resistance when drugs do enter the brain, and attenuated anti-tumour immunity, particularly in brain metastases originating from breast cancer[1, 2].

The lack of progress in treating established breast cancer brain metastases has led to a call for approaches to prevent the initial metastasis or additional metastases once a single, treatable lesion is apparent[3]. The latter has become an innovative clinical trial paradigm[3], but approaches to prevent brain metastasis altogether have been hampered by the prevailing notion that the steps that are rate limiting are the ones that are unfeasible to target (e.g., extravasation)[4–6]. As a result, less consideration has been given to approaches to prevent brain metastasis by setting our sights on a more practical target: dormant disseminated

tumour cells (**DTCs**). This is particularly notable because the current prevalence of breast cancer brain metastasis (up to 30.8% of women with metastatic triple negative breast cancer, **TNBC**[7], for example) is in sharp contrast to its rarity a century ago[8]. This increase in frequency over the last 100+ years might reflect a situation where breast tumour cells that disseminated to the brain and remained dormant until the patient succumbed to metastasis elsewhere now have more time to evolve into clinically detectable disease due to application of effective systemic therapy[1].

This theoretical explanation is supported by empirical observations in humans, where a detailed autopsy study of cancer patients uncovered single DTCs in the brains or livers of 96% of subjects[9], and in mice, where iron oxide labeled TNBC cells tracked for four-weeks by magnetic resonance imaging revealed that single DTCs co-exist with brain metastases[10]. Presence of single DTCs has been confirmed up to 10 weeks after inoculation of human breast cancer cell lines in immune compromised mice[4]. We have shown that such cells are situated within the vascular niche[11]. But unlike bone marrow[11, 12], where the perivascular locale of quiescent DTCs hinted at molecular mechanisms of dormancy that may be operative in humans[13], this finding appeared at odds with literature suggesting that occupation of the brain's vascular niche is required for metastatic progression. For example, detailed fate-maps of melanoma and lung cancer cell lines in immune compromised mice demonstrated that occupying the abluminal surface of the vasculature is required for survival in brain[14], studies in zebrafish and chick embryos demonstrated that gap junction communication between breast cancer or melanoma cells and endothelium is an early and critical step for brain metastasis formation[15], and two studies showed that integrin-β1-mediated adhesion to the vascular niche is required for brain metastatic progression[16, 17]. Further exploration revealed that breast cancer cell adhesion and spreading upon microvasculature in the murine brain are initiated by the cell adhesion molecule L1CAM, involve competition with pericytes for this real estate, and require integrin-β1 activation and nuclear shuttling of yes associated protein-1 (**YAP**) to promote brain colonization[17]. Together these studies implicate activation of integrin-β1 and YAP for brain colonization. But what prevents cells from exiting dormancy? Is dormancy simply a default state defined by lack of engagement/activation of L1CAM, integrin-β1 and downstream mediators? Or are active mechanisms in place, perhaps employed already under physiologic conditions to enforce quiescence?

In addition to endothelial cells, the brain's vascular niche is comprised of perivascular cells including astrocytes and pericytes, which operate in concert with endothelium to build physical and chemical barriers that are critical for proper brain physiology[18, 19]. The role of resident pericytes in brain metastasis has not been studied extensively. In contrast, a wealth of evidence spanning 90 years indicates astrocytes reprise the role they play during local insults by undergoing astrogliosis and exhibiting a "reactive" phenotype over the course of brain metastatic progression[20]. This is accompanied by dramatic changes in astrocyte morphology, including hypertrophy, altered ramification and withdrawal of endfeet from the vasculature, thereby disrupting the BBB[21]. But these changes are not merely passive. Reactive astrocytes promote tissue colonization through secretion of chemokines and other soluble factors including neurotrophins[22], heparinase[23] and CXCL10[24], and by exosomal

micro-RNA cargos that downregulate the tumour suppressor PTEN in DTCs[25]. Again, in this context, it is unclear if dormancy is simply failure to induce astrocyte reactivity, or if astrocytes somehow contribute to a suppressive microenvironment under homeostatic conditions.

Here, we employ serial intravital microscopy to contrast TNBC cells that do and do not form brain metastases, revealing that dormancy is the rate limiting step of brain metastatic progression. We confirm that DTCs that remain dormant for several weeks and DTCs that rapidly colonize the brain both occupy vascular niches. More detailed analysis of the perivasculature, however, reveals that astrocytes and their endfeet are stripped from vessels as micrometastases become proliferative. To identify a putative astrocyte-derived tumour suppressor, we employ a combination of culture-based mimetics of the brain's perivascular niche, extracellular matrix (**ECM**) focused proteomics, and nestin-driven transgenic knockout mice and demonstrate that astrocytes suppress breast cancer cell proliferation via contributions (namely, Laminin-211) to the brain's parenchymal basement membrane. Our studies of potential Laminin-211 receptors reveal that astrocytic laminins signal through dystroglycan, which physically associates with and negatively regulates nuclear shuttling of the pro-proliferative transcriptional activator YAP to enforce DTC quiescence. These findings provide insight into the unique cellular and molecular context that drives DTC quiescence in brain, and set the foundation for approaches to maintain this state and/or target the seeds of brain metastases before they have a chance to sprout.

Results.

Dormancy is rate-limiting for breast-to-brain metastasis.

A number of steps have been proposed previously as rate-limiting for brain metastasis, spanning survival upon arrest within the brain microvasculature[4], extravasation through the BBB[5], and persistence of DTCs within a 'foreign' microenvironment[6]. The contribution of DTC dormancy—long assumed to be rate-limiting— is undefined. The ability to apply intravital imaging to revisit this issue in brain by direct comparison of parental lines that rarely form brain metastases with syngeneic, brain-metastatic derivatives offered an approach to document exactly where parental lines were limited.

We identified two breast cancer cell (**BCC**) lines that disseminate to the brain, but only rarely generate metastases: HMT-3522-T4-2 (**T4-2**) and MDA-MB-231. Both are triple-negative BCC lines (i.e., they do not express estrogen- and progesterone- receptors; and lack HER2 amplification) and are relevant to the study of dormancy because TNBC is now a prime contributor to breast cancer brain metastasis[7]. To understand where in the metastatic cascade these lines most commonly failed, it was necessary to contrast them with brain metastatic counterparts. Therefore we derived a brain metastatic subline of T4-2 (**T4-2-BR1**) and obtained a brain metastatic derivative of MDA-MB-231 (**MDA-MB-231-BR7**[26]). Each was inoculated into NOD-SCID mice fitted with an intravital imaging window, and tracked over subsequent weeks using vascular 'landmarks' to record the fate of individual DTCs every three to four days via two-photon imaging (Fig. 1a). This method, established originally by Kienast et al[14], allowed us to track individual DTCs as they arrived and

extravasated into the brain, died, became dormant or underwent metastatic progression (Fig. 1b-e).

The majority of cells (805 of 903 cells tracked) that arrived in the brain died, either pre- or post-extravasation, in both models. Parental T4-2 cells and T4-2-BR1 were no different in this regard; both exhibited similar rates of intravascular death or displacement (60.8% vs. 59.7%) and death at any point after extravasation from dextran-labeled vasculature (51.6% vs. 53.8%; Fig. 1f). Despite seven generations of selection for brain tropism, MDA-MB-231-BR7 did not differ drastically from their parental counterparts in this respect, either, with an 11% decrease in intravascular death and a similar (10.1%) decrease following extravasation (Fig. 1g). Nor did these lines differ markedly in their ability to navigate the BBB. Out of 316 T4-2 cells tracked, 39.2% successfully extravasated into brain, compared to 40.3% of T4-2-BR1 (Fig. 1f). MDA-MB-231-BR7 outperformed MDA-MB-231 based on this metric, extravasating 18.3% more efficiently than the parental line (Fig. 1g). But these modest rates were insufficient to account for the increase in metastases observed with both sublines (Fig. 1d-g). Far larger differences in both pairs were evident when observing the rate at which they entered and sustained dormancy on a single cell- (Fig. 1b, c, f, g) or micrometastatic- level. Brain metastatic T4-2s exhibited a 56.6% decrease in the fraction that became dormant, whereas *no* MDA-MB-231-BR7 were observed in this state (Fig. 1f, g). The efficiency by which T4-2-BR1 formed micrometastases was 2.39-fold greater than the parental line (Fig. 1f, Extended Data Fig. 1c), whereas MDA-MB-231-BR7 were 3.34-times more efficient than MDA-MB-231 at progressing to this state (Fig. 1g, Extended Data Fig. 1d). The largest difference between the two lines was their ability to sustain, and eventually escape from the micrometastatic state. Whereas nearly all parental T4-2 and MDA-MB-231 regressed upon forming micrometastases (meaning they either died or regressed back to the single cell level, Extended Data Fig. 1 a, b, e), only 31.2% of T4-2-BR1 and 3.4% of MDA-MB-231-BR7 micrometastases met this fate (Fig. 1f, g). Similarly, one-quarter (vs. 0%) and 96.6% (vs. 0%) of T4-2-BR1 and MDA-MB-231-BR7 were able to form full-blown metastases (Fig. 1d-g).

With the caveat that we cannot state with any certainty what the predominant fate of lines we have characterized as dormant would have been over longer tracking periods, these data suggest that the bottleneck to brain metastasis is not entry into the brain or survival once there, but the ability to sustain escape from the single cell state. This emphasizes the need to understand how dormancy of DTCs and of micrometastases is enforced, and what factors lead to its diminution.

Astrocyte endfeet are stripped from vessels upon DTC activation.

Prior studies suggest the brain's vascular basement membrane is a substratum for L1CAM and integrin-β1-mediated spreading and activation of DTCs[16, 17]. This description is seemingly at odds with the finding that dormant DTCs also occupy a perivascular niche[4, 11, 14, 17]. We asked whether parental lines that do not proliferate over the course of several weeks differ from brain metastatic derivatives in the niches they occupy. We found that all 564 cells that successfully extravasated into brain across all four models occupied a perivascular niche, defined by physical association with the abluminal surface

of TRITC-Dextran perfused microvasculature (Fig. 1b-g). Therefore we wondered if other components of this niche play a more obvious role in enforcing the dormant state.

Perivascular cells in brain include astrocytes and pericytes, which participate in molecular crosstalk to induce expression of endothelial tight junction molecules, manifesting in formation of a physical BBB[18, 19, 27]. Specialized astrocytic structures called endfeet ensheath the brain's microvessels and add to barrier function through arrayed aquaporin-4 (**AQP4**) channels that regulate water influx and hence ion concentration[28]. AQP4 is localized to the surface of endfeet juxtaposed to the abluminal surface of endothelium by the dystroglycan-dystrophin complex[28], which is tethered to the second of two basement membranes (the vascular basement membrane being the first) surrounding the brain's microvasculature. This parenchymal basement membrane is rich in astrocyte-derived glycoproteins laminins-211 and −111 and the proteoglycan agrin[27, 29, 30]. Deletion of astrocytes, pericytes, lama2 or agrin is sufficient to disrupt polarization of astrocyte endfeet, endothelial tight junctions, and overall barrier function[18, 19, 31, 32]. With this background, we surmised that studying localization of astrocytes and pericytes over the course of brain metastatic progression might provide clues as to how DTC dormancy is regulated within the perivascular niche.

It has long been established morphologically that astrocytes are 'stripped' from the vasculature and segregated to the border of brain metastases[33, 34]. Still, we were surprised to observe how early in metastatic progression this occurred. Vasculature adjacent to quiescent (i.e., Ki67-negative) T4-2 DTCs was ensheathed by $AQP4^+$ endfeet, and only a marginal (15%) reduction in coverage was observed in vessels bordering Ki67-negative micrometastases (Fig. 2a-c). A profound reduction (85%) in endfoot coverage was evident in even small micrometastases containing a single Ki67-positive cell, and these structures were almost totally removed from vessels within brain metastases (Fig. 2b-c). Loss of $AQP4^+$ endfeet in this model coincided with a drastic reduction in perivascular, $GFAP^+$ astrocytes (Extended Data Fig. 2a-b), indicating that astrocyte eviction coincided with endfoot removal.

Because deletion of $Pdgfrb^+$ pericytes disrupts AQP4 polarization and phenocopies endfoot removal[19], we also measured PDGFR-β coverage of DTC-associated vessels over the course of metastatic progression. Here, we noted no significant differences in pericyte coverage of vessels adjacent to quiescent DTCs, micrometastases or metastases (Fig. 2d-e). Examination of metastatic progression in the MDA-MB-231 model revealed a very similar phenomenon: there was a 79% reduction in astrocyte endfoot coverage of micrometastasis-associated vessels upon transition from Ki67-negative to Ki67-positive, but no significant loss of pericyte coverage at this stage, and no further exacerbation of pericyte loss upon progression to full-blown metastases (Fig. 2f-i).

The critical role for astrocyte endfeet in maintaining BBB physiology and the coincidence of endfoot stripping at the earliest stages of DTC proliferation led us to suspect that astrocytes might play a role in suppressing DTC outgrowth in brain.

Astrocytes suppress breast tumour cells via laminin-α2.

To conduct gain- and loss- of function experiments with astrocytes as the sole variable, and ultimately to pinpoint potential means by which they might suppress breast tumour cell outgrowth, we created a culture-based mimetic of the brain's perivascular niche consisting of primary human brain adventitial fibroblasts (**HBAF**s), and human endothelial cells engineered to survive in serum- and cytokine-free conditions[35]. The addition of endothelium to brain fibroblasts, a perivascular population identified recently in mice[36] and in humans[37], resulted in formation of a microvascular network (Fig. 3a-b). Addition of T4-2 or MDA-MB-231 cells to these niches led to a modest and statistically significant 25.7% reduction of outgrowth in the T4-2 model (Fig. 3b-c), but had no impact on MDA-MB-231 proliferation (Extended Data Fig. 3a-b). And unlike what we had documented previously for bone marrow and lung[11], the addition of endothelium did not drive either cell line into a quiescent state, given the non-significant differences between Ki67-negative fractions of either BCC line in cultures containing only HBAF or HBAF and endothelial cells (Fig. 3d; Extended Data Fig. 3c).

The addition of astrocytes to cultures containing HBAF and endothelium suppressed T4-2 and MDA-MB-231 breast tumour cell outgrowth significantly compared to HBAF, or HBAF and endothelial cell cultures (Fig. 3b-c, Extended Data Fig. 3a,b). This coincided with a near doubling of the fraction of $Ki67^-$ (quiescent) cells in both cultures compared to HBAF alone (Fig. 3d, Extended Data Fig. 3c). Experiments where the concentration of either endothelial cells or astrocytes was held constant while the other was increased confirmed that the burden of suppression lay with astrocytes (Extended Data Fig. 3d,e). Interestingly, the full combination of HBAF, endothelium, and astrocytes was necessary for suppression. Either cell type on their own, or any pairwise combination did not suppress outgrowth when compared to cultures consisting solely of HBAFs (Extended Data Fig. 3f). This suggested that in culture, breast tumour cell suppression manifests from association of astrocytes with properly organized endothelium.

What drives this suppression? The observation that dormant DTCs physically contact $AQP4^+$ astrocyte endfeet in vivo (e.g., Fig. 2b,f) suggested that the putative tumour suppressor(s) was not freely diffusible. Conditioned media experiments confirmed this assertion (Extended Data Fig. 3g). Therefore, to identify insoluble factors deposited by astrocytes into the brain's perivascular niche, we compared differentially expressed ECM molecules between brain vascular niche cultures and other culture-based perivascular niche mimetics developed in our lab (lung, bone marrow and liver) by quantitative profiling of ECM. This revealed a number of ECM molecules unique to brain perivascular niches (Fig. 3e). Among these, we identified 24 that were enriched 1.5-fold when astrocytes were present (vs. HBAF and endothelium alone; Fig. 3f). To determine if any of these putative astrocyte-derived factors suppressed breast tumour cell outgrowth on brain fibroblasts, we conducted a gain-of-function screen by expressing 18 of these ECM molecules in HBAF (we were unable to clone the other six successfully). Among 18 overexpressed ECM proteins, versican, collagen XVIII, agrin and laminin-α2 significantly and substantially reduced outgrowth of T4-2 cells to <=47% of control (empty pLX304 vector) despite absence of endothelium and astrocytes (Fig. 3g-h).

Mining publicly available transcriptomic data[38] revealed that of these four ECM proteins, only laminin-α2 was expressed predominantly by astrocytes in murine brain (Extended Data Fig. 4a). This drew our attention to laminin-α2. Laminins are a family of 16 trimeric proteins composed of α−, β− and γ− chains; laminin-α2 is a constituent of three such proteins, laminin-211, −213 and −221 [39]. Whereas endothelial cells and to a lesser extent pericytes contribute two unique laminins (laminin-411 and laminin-511) to the vascular basement membrane[29], laminin-211 (comprised of the products of the lama2, lamb1 and lamc1 genes) and −111 are the major laminins produced by astrocytes and deposited into the brain's parenchymal basement membrane[31]. Therefore, to assess whether suppression was limited to laminin-211 or shared more broadly amongst these laminins, we added increasing amounts of purified laminin-211, −111, −411 and −511 to brain fibroblasts, and measured BCC outgrowth over time. Only laminin-211 significantly and substantially reduced T4-2 cell outgrowth (to 44% of control) at 5 μg/ml (Fig. 3i, Extended Data Fig. 3h). Both astrocytic laminins reduced outgrowth at 10 μg/ml; laminin-411 and −511 did not impact BCC outgrowth at any concentration tested (Fig. 3i, Extended Data Fig. 3h). These data pinpoint astrocytic laminins, especially laminin-211, as potential drivers of DTC dormancy in brain.

Perivascular laminin-211 diminishes during brain colonization.

To test the hypothesis that astrocytic laminin-211 is associated with quiescent DTCs in humans, we analyzed sections adjacent to those where we had identified $HER2^+$ DTCs in grossly uninvolved brain of a stage IV, $ER^+/PR^+/HER2^+$ breast cancer patient who succumbed to her disease, from a metastatic lesion within the same patient's brain, and from surgically resected breast cancer brain metastases from 22 individual cases (Supplementary Table 1). DTCs and metastases were identified by layering Cytokeratin-7 and Her2 on the same channel[40]. We quantified laminin-α2 coverage of DTC-associated vessels and vessels within metastases, using values obtained from brain microvasculature of five subjects with no documented history of cancer as a control. We found four $Ki67^-$ DTCs or micrometastases in the rapid autopsy specimen, all physically associated with laminin-$\alpha2^+$ microvessels (Fig. 4a,c). On the other hand, laminin-α2 was largely depleted from $CD31^+$ structures contained within brain metastases (Fig. 4b,c). Quantification of laminin-α2 across lesions revealed a 74.8%−82.3% reduction of laminin-α2 coverage when compared to $CD31^+$ vessels sampled within normal brain, vessels associated with $Ki67^-$ DTCs/micrometastases, and vessels in 'normal' brain adjacent to metastases (Fig. 4a-c).

This finding was consistent with what we observed over the course of metastatic progression in NOD-SCID mice inoculated with T4-2 and MDA-MB-231 cells, where loss of perivascular laminin-α2 coincided with DTC proliferation (Fig. 4d,e, Extended Data Fig. 4b). Indeed, examining vasculature within metastases and just outside of the metastatic border revealed that laminin-α2 was stripped from vessels within metastatic lesions, but present immediately outside of its borders (Extended Data Fig. 4d). This pattern was not observed with the other astrocytic laminin, laminin-111, which was retained within metastases at levels equivalent to the regions neighboring metastases (Extended Data Fig. 4c,d).

Altogether these data hint that astrocytic laminin-211 may drive and sustain DTCs in a quiescent state. But we desired a loss-of-function approach in vivo to test this hypothesis more directly.

Knockout of astrocytic laminin-γ1 promotes brain metastases.

To test whether astrocytic laminin-211 drives DTC quiescence in vivo, we adopted a strategy defined previously to result in astrocyte-specific ablation of laminin-211 [41]. Here, our experimental model was achieved by crossing Nestin-Cre, Lamc1$^{flox/+}$ heterozygous mice with homozygous Lamc1$^{flox/flox}$ mice (called **N-γ1-KO** from here on out; Fig. 4f). Nestin is expressed by neural progenitors, which differentiate into neurons and astrocytes in the late embryo stage[42]. Because laminin-γ1 chain deletion prevents self-polymerization of γ1-containing laminins[43], laminin-211 and −111 are theoretically deficient in both neurons and astrocytes in these mice. We assessed loss of perivascular laminin-211 in this model and documented substantial depletion of laminin-γ1, and spotty, mosaic depletion of laminin-α2 that nonetheless did not manifest as a statistically significant reduction (Fig. 4g,h).

Expression of fluorescent proteins, necessary to detect and measure metastatic burden accurately, trigger immune responses in immune-competent mice like the transgenics employed for these experiments[44]. Therefore, one extra cross was necessary to ensure that experiments in this model would not be hampered by any potential artefacts introduced by expressing a fluorescent protein (namely, tdTomato) in transplanted tumour cells. Therefore, we crossed N-γ1-KO mice with Cx3cr1-GFP;CCR2-RFP mice to generate tdTomato tolerized N-γ1 KO mice, and used the presence/absence of the leukocyte marker CD45 to distinguish tdTomato^{+} tumour cells from RFP^{+} monocytes. Syngeneic, tdTomato^{+}, triple-negative mammary cancer cells (E0771) were then delivered to tolerized N-γ1 KO mice or their control littermates via intracardiac injection (Fig. 4i).

These experiments were terminated only 13-days later because a subset of these mice displayed severe neurologic symptoms. Imaging whole brains at this timepoint revealed that all N-γ1 KO mice inoculated with tdTomato-E0771 developed more numerous and larger metastases than their littermate controls (Fig. 4j). Inspection of brain sections spanning the entire brain (10% of the brain represented on each slide, in sum) showed a 4.6-fold increase in the number of metastatic lesions in N-γ1 KOs, accompanied by a 3.5-fold increase in the average size of each lesion (Fig. 4k,l). Importantly, because we noted reduced AQP4 coverage of microvessels in the brains of N-γ1 KO mice (Extended Data Fig. 5a,b) we confirmed that increased metastasis in N-γ1 KOs was not due simply to increased extravasation following inoculation of E0771 cells. Quantifying DTC concentration only 3 days after intracardiac inoculation revealed that the number of tumour cells occupying the brain at this early timepoint was similar in N-γ1 KOs and their littermates (Extended Data Fig. 5c-e). We noted also that the impact of nestin-driven laminin-γ1 loss on metastatic outgrowth was specific to the brain; we did not document an obvious effect of N-γ1 KO on ovary or lung metastasis (Extended Data Fig. 5f-h).

In summary— in full context of the data derived from culture-based mimetics of the brain's perivascular niche— the dramatic promotion of brain metastasis in N-γ1 KO mice paints astrocytic laminin-211 as a dominant enforcer of DTC quiescence in brain.

DTC dystroglycan mediates suppressive cues from laminin-211.

Laminin-211 engages three receptors: integrin-$\alpha_6\beta_1$ and integrin-$\alpha_7\beta_1$, and the non-integrin receptor dystroglycan, encoded by *DAG1* [39, 45]. Whereas previous work demonstrated that clustering of integrin-β_1 drives disorganization and malignant outgrowth of mammary epithelium[46] while also promoting outgrowth at metastatic sites including brain[16, 17], the role of dystroglycan in DTC biology remains undefined. So we took a loss-of-function approach to explore whether DTC dystroglycan or integrins were important for interpretation of suppressive cues from astrocytic laminin-211 (Fig. 5a).

Because integrin-α_7 was expressed negligibly at the transcript level by the cell lines employed in this study we used shRNA to knockdown *DAG1, ITGA6,* or *ITGB1* in parental T4-2 cells, which persist within brain as dormant DTCs and micrometastases, but rarely generate brain metastases (Fig. 1b). Knockdown of dystroglycan α− and β− domains was assessed by western blot, and two clones (clones 2 and 4) that achieved >52% knockdown of the dystroglycan β−domain were selected (Fig. 5b-d). To facilitate comparison, we identified two clones that resulted in knockdown of the integrin-α_6 subunit by 48% (clone 3) and 76% (clone 5), and another that achieved 83% knockdown of integrin-β_1 (Fig. 5b-d).

T4-2 cells infected with shDAG1 (Cl. 2 or Cl.4), shITGA6 (Cl. 3 or Cl. 5), shITGB1, or their respective controls were delivered to NOD-SCID mice via intracardiac injection. Nearly three-quarters of mice inoculated with shEmpty T4-2 cells either failed to develop detectable lesions, or developed a single micro-metastatic lesion over the next six-weeks (Fig. 5g-i). In contrast, 23/26 mice (>88%) inoculated with shDAG1 T4-2 cells had lesions in their brain that were detectable ex vivo by whole brain imaging over an identical time course. Inspection of brain sections showed a 5.1–6.9-fold increase in the number of metastatic lesions upon *DAG1* knockdown (Fig. 5g,h). The average size of these more frequent lesions was also far greater and scaled with the level of knockdown of the dystroglycan β-domain (Fig. 5i).

In contrast, the impact of *ITGA6* knockdown on T4-2 brain colonization was not as robust as observed upon knockdown of *DAG1*. Whereas one clone (Cl. 3) drove a three-fold increase in the overall number of metastatic lesions, the other (Cl. 5) had no effect in this regard (Fig. 5j,k). Neither affected the average lesion size in a statistically significant fashion (Fig. 5l). These data could be interpreted to mean that integrin-α_6 might restrict initial outgrowth of brain disseminated T4-2 cells, but that its loss confers no advantage in colonizing this organ. Finally, mice inoculated with shITGB1 T4-2 failed to develop any visible brain metastasis, resulting in a total absence of lesions in these mice (Fig. 5m-o). This result is consistent with previous findings that integrin-β_1 promotes metastatic outgrowth within brain[16, 17].

These data indicate that dystroglycan is the dominant receptor of DTC-suppressive cues in the brain. We went a step further to determine whether this holds true in immune-competent settings, and to identify whether laminin-211 is its primary ligand. We inoculated syngeneic, RFP-tolerized N-γ1 KO mice or their control littermates with tdTomato-E0771 cells expressing either non-targeting shRNA or shRNA targeting *Dag1* (Extended Data Fig. 6a-b). The rationale was that the metastasis promotion observed upon *Dag1* knockdown or

Lamc1 deletion in nestin-expressing cells should be saturated if dystroglycan is indeed the key receptor for astrocytic laminins; i.e., combination of the two should not produce an additional advantage. Our results were consistent with this reasoning. Mice inoculated with E0771 cells expressing non-targeting shRNA showed a 9-fold increase in the number of metastatic lesions in N-γ1 KOs, accompanied by a 3.3-fold increase in the average size of each lesion (Extended Data Fig. 6c-g). In line with data derived from T4-2 inoculation into immune-compromised hosts, dystroglycan knockdown promoted brain metastatic outgrowth in control mice, with a 4.3-fold increase in lesion number and 2.7-fold increase in total metastatic burden (Extended Data Fig. 6c-g). But in the context of N-γ1 KO, dystroglycan knockdown did not confer any kind of advantage for brain colonization as measured by total lesion size, number of lesions per section or average lesion size (Extended Data Fig. 6e-g). Taken together, data from these two different experimental models identify dystroglycan as the dominant receptor for transduction of suppressive cues from astrocytic laminin-211.

YAP signaling is suppressed in dormant DTCs.

We designed a single cell sequencing experiment to gain an understanding of potential mechanisms by which dystroglycan could effect DTC quiescence (Fig. 6a). We dissected, digested and flow-purified tumour cells from brain metastases generated via inoculation of NOD-SCID mice with a tdTomato-positive, brain metastatic variant of T4-2 cells ("Macromet," Fig. 6b). In parallel, remaining uninvolved brain was digested, and residual tdTomato^{+} tumour cells were purified from this digest via flow ("Micromet," Fig. 6b; see Extended Data Fig. 7 for gating scheme). In total, 3,973 cells from brain metastases and 1,252 DTCs from uninvolved brain were transcriptionally profiled via single cell RNA sequencing.

Uniform manifold approximation and projection (**UMAP**)-based dimensional reduction and graph-based Leiden clustering identified 10 distinct populations from these data (Fig. 6c). Indices allowed us to examine how these populations were distributed between brain metastases and micrometastases. The majority of populations were present in both metastases and micrometastases, and expanded in the former. But there were three notable exceptions: Cluster 0, which was exclusive to metastases; Cluster 2, which expanded drastically within metastases; and Cluster 5, which was exclusive to the micrometasases isolated from grossly uninvolved brain (Fig. 6d). We selected differentially expressed genes unique to each of these clusters (Supplementary Table 2), and conducted gene set enrichment analysis using the STRINGdb database to connect gene products within each cluster by highest confidence interacting partners (Fig. 6e-f). Analysis of genes enriched within each of these clusters suggested Cluster 0 may reflect bioenergetic requirements for brain metastasis, whereas Cluster 2 was enriched for cell cycle related genes and was likely a proliferative population contained principally within metastases (Fig. 6e-f). Cluster 5, on the other hand, was enriched by a network of genes comprising Hippo pathway signaling (Fig. 6e-f).

The Hippo pathway is an evolutionarily conserved serine kinase cascade with associated regulatory and scaffolding proteins that control cellular growth and organismal size. Its principal growth regulatory function is executed by preventing nuclear accumulation of

YAP, which otherwise activates a suite of proliferation associated genes (in part) through association with the TEAD transcription factors[47]. Assessment of a curated "YAP target gene score" spanning 22 YAP targets[48] from the single cell data confirmed statistical enrichment for these genes in Cluster 0, which was also significantly enriched for MKI67 (the gene encoding Ki67) when compared to Cluster 5 (Fig. 6g). Indeed, analysis of YAP target gene score as a function of cell cycle across all cells/clusters showed a positive correlation with S- and G2/M- phases, and strong anticorrelation with quiescence[49] (Fig. 6h). The implication of these data was confirmed by immunofluorescent staining; YAP was absent from the nucleus of solitary, Ki67-negative DTCs and exhibited strong nuclear localization in proliferative micrometastases and metastases in the T4-2/NOD-SCID model and in E0771 brain metastases resulting from *Dag1* knockdown and/or inoculation of N-γ1 KOs (Extended Data Fig. 8a-d). Whereas these data confirmed a compelling, previously documented association between YAP and brain colonization[17], we sought to determine whether nuclear exclusion of YAP in dormant DTCs was somehow tied to laminin-211-DAG signaling.

Dystroglycan may effect DTC quiescence by tethering YAP to the cell membrane.

The β-domain of dystroglycan contains motifs predicted to interact physically with the conserved WW domain of YAP[50]. Indeed, recent evidence from cardiomyocytes and skeletal muscle cells suggests dystroglycan could play a role in YAP inactivation, effectively sequestering Ser 127 phosphorylated YAP (pYAP (S127)) from the nucleus[51]. To understand whether a similar mechanism is operative in quiescent DTCs, we probed for a physical interaction between YAP and dystroglycan via proximity ligation assay (**PLA**), a sensitive method to detect protein-protein interactions via proximity-dependent hybridization and amplification of oligonucleotide-bound antibodies (Fig. 7a)[52]. Single, disseminated T4-2 cells probed with dystroglycan or YAP antibody alone generated no PLA signal, as expected (Fig. 7b). We detected signal in normal brain when applying both antibodies, suggesting that mechanisms uncovered in skeletal muscle and in cardiomyocytes[51] might apply here, too (Fig. 7b). Examination of disseminated breast tumour cells revealed strong PLA signal confined to the interface of single DTCs with adjacent cells; signal was rarely detected in micro-and macro-metastatic lesions (Fig. 7c), consistent with the hypothesis that dystroglycan binds and sequesters YAP to the membrane of quiescent DTCs, and that this tethering is lost upon proliferation. YAP pulldown hinted that this interaction could be enhanced by astrocytic laminin, as the amount of β-dystroglycan bound to YAP was enhanced 2.3-fold by culture on laminin-211 (Extended Data Fig. 8e-f).

We went on to test whether YAP activation is sufficient to drive outgrowth of quiescent DTCs despite functional dystroglycan. YAP activity is regulated by nuclear translocation; once phosphorylated at S127 by Hippo effectors, it is confined to cytoplasm where it can be phosphorylated further at S397 and targeted for degradation[53, 54]. So we overexpressed two forms of constitutively active YAP in T4-2 cells: the S127A mutant, where serine 127 is mutated to alanine and therefore YAP shuttles freely to the nucleus, and the S127A/S397A mutant, where serine 397 is also mutated to alanine and YAP is effectively protected from the phosphodegron[54]. In parallel, we expressed a loss of function YAP mutant (S94A) that cannot interact with its transcriptional co-activator TEAD[55]. Expression of each mutant was

confirmed by western blot (Fig. 7d,e). The S127A mutant overrode functional dystroglycan and resulted in a prolific enhancement in the number and size of brain metastases. The S127A/S397A double-mutant promoted brain metastasis equivalent to the S127A single mutant, but not beyond (Fig. 7f-h). YAP that could not activate transcription via TEAD had no effect on either parameter (Fig. 7f,h). In sum, the YAP mutant (S127A) that regulates nuclear shuttling and thus overrides the hypothesized function of dystroglycan promotes escape from dormancy and brain colonization, and preventing ubiquitination/degradation of YAP (via S397A mutation) does not confer an additional advantage. These data are consistent with a function for intact, laminin-bound dystroglycan sequestering YAP from the nucleus and driving DTC quiescence.

We wondered also whether YAP depletion was sufficient to blunt the metastatic phenotype observed upon dystroglycan knockdown (Fig. 5). Once inoculated in NOD-SCID mice, YAP knockdown inhibited outgrowth of T4-2 cells commensurate to the level of YAP depletion (Fig. 7i-m). Together, these data reveal a mechanism whereby dormancy is enforced actively via astrocytic laminin-211 signaling through DTC dystroglycan to effect quiescence by cytoplasmic sequestration of YAP. Disruption of this axis at any level is sufficient to break DTC quiescence and catalyze emergence of metastases in a manner specific to the brain (Fig. 7n).

Discussion.

Through a combination of intravital imaging, mouse modeling, high-dimensional profiling and functional studies in culture-based mimetics of the brain's perivascular niche, we show that: i) escape from dormancy at the single cell or micrometastatic level is the rate limiting step of brain metastasis, ii) dormant and proliferative DTCs occupy distinct niches defined by whether or not they are associated with astrocyte endfeet; iii) astrocytes stimulate quiescence via deposition of laminin-211 into the parenchymal basement membrane, which iv) transduces pro-dormancy signaling via the non-integrin receptor dystroglycan, and v) promotes quiescence through cytoplasmic sequestration of YAP, thereby preventing YAP from activating growth-promoting programs that appear critical for brain metastasis (Fig. 7n)[17]. The lack of an overt phenotype in any other organ upon Nestin-driven deletion of *lamc1* or upon knockdown of tumoural dystroglycan suggests this mechanism is tissue-specific.

These findings are illustrative that mechanisms that drive DTC dormancy are likely to be molecular frameworks already in place for normal tissue physiology. In brain, the dystroglycan-associated protein complex must engage components of the parenchymal basement membrane, including laminin-211, for proper organization and localization of AQP4 channels to the correct surface of astrocyte endfeet[28]. This serves a critical barrier function, as disruption of this complex compromises water transport into brain[28, 31, 41]. Our data reveal that this signaling is 'co-opted' by DTCs in vascular niches containing astrocytic endfeet, and induces signaling that steers them into a quiescent state. It is likely that in other organs, preexisting, spatially-restricted mechanisms are co-opted for dormancy regulation as well.

It is apparent from examination of tissue pathology that perivascular laminin-α2 is lost within proliferative brain metastases (Fig. 4a-c), but when and how this suppressive cue diminishes over the course of disease in humans remains an open question. Local insult— whether by trauma, stroke, virus, or neural degeneration— causes astrocytes to undergo astrogliosis and become reactive. This process is accompanied by dramatic changes in astrocyte morphology, including hypertrophy, altered ramification and endfoot depolarization and withdrawal[21]. Therefore one way DTCs might emerge after a prolonged period of dormancy is that astrocytes in the vicinity of DTCs are activated by local neural damage or infection-associated inflammation. Indeed, in lung inflammation is sufficient to cleave laminin-111 and promote the very type of integrin-β1 and YAP-mediated signaling required for tissue colonization[56]. Perhaps in brain similar mechanisms are operative and lead to the destruction of laminin-211.

A better understanding of these mechanisms will be necessary to convert dormancy from a biological phenomenon to an exploitable therapeutic window[57]. One approach is to sustain DTCs in a dormant state. Perhaps an approach that agonizes dystroglycan function by promoting its glycosylation[58] and capacity to bind astrocytic laminins can accomplish this. An alternative approach is to uncover DTC vulnerabilities that result in their eradication. In this vein it is notable that DTCs emerging from dormancy often fail to colonize brain and regress (Extended Data Fig. 1a,e). This may indicate a vulnerability to this transition phase. Understanding this would be aided substantially by wholesale documentation of how the DTC niche evolves in time and space to leverage this biology for therapeutic intervention.

Methods.

Animal studies.

All animal work was performed in accordance with institutional Fred Hutchinson Cancer Research Center (Fred Hutch) approved IACUC protocols 51075, 51076 and 50928, and AAALAS guidelines and ethical regulations. All animals were kept in a controlled environment with12/12h light/dark cycle, temperatures of 65–75°F (~18–23°C) and 40–60% humidity. Nestin-cre (B6.Cg-Tg(Nes-Cre)1Kln/J; 003771)[59], Lamc1fl/fl (B6.129P2-Lamc1^{tm1Strl}/J; 016917)[60], Cx3cr1GFP;Ccr2RFP(B6.129(Cg)-Cx3cr1^{tm1Litt} Ccr2$^{tm2.1Ifc}$/JernJ; 032127) [61] mouse strains were on a C57BL/6 background and obtained from the Jackson Laboratory. NOD SCID (NOD.CB17-Prkdc^{scid}/NCrCrl; 394) mice were purchased from Charles River. For all animal experiments, six to eight-week-old females were used.

Craniotomy surgery and cranial window installation.

Six to eight-week-old female NOD SCID mice were anesthetized by isoflurane and the upper portion of the skull was surgically removed. Glass coverslip ‘windows’ (diameter ~5 mm) were implanted as described previously[14], with a custom-made titanium ring to reduce animal discomfort and stabilize the head during imaging. Mice were allowed to recover under mild heat, then rested for 21 days to relieve surgery-induced gliosis and inflammation prior to tumor cell injection. Mice that developed blood clots and/or extensive bone regrowth after 21 days were removed from the study group.

Ultrasound-guided intracardiac injection.

Twenty-one days after craniotomy, mice were anesthetized and positioned in dorsal recumbency on a Visual Sonics Vevo 2100 Ultrasound Imaging System. 1×10^6 eGFP-expressing HMT-3522-T4-2 (**T4-2**)[62] or 5×10^5 eGFP-MDA-MB-231[63] breast cancer cells and their respective brain-tropic sublines (T4-2-BR1 and MDA-MB-231-BR7 [26, 64] were passed through a 70 μm nylon mesh filter twice to ensure a single cell suspension, then resuspended in 100 μl volume PBS and guided into the left ventricle of the heart with a 26 ½ gauge needle via ultrasound. Needle height and angle was adjusted on a stereotactic rig. The cell suspension was injected slowly after visualizing blood reflux into the syringe.

In vivo multiphoton laser scanning microscopy (MPLSM) and analysis.

MPLSM imaging was conducted using a Zeiss 7MP microscope (Zeiss) equipped with a pulsed Ti:Sapphire laser (Chameleon II ultra; Coherent). The following wavelengths were used for excitation: 850 nm (GFP), and 950 nm (TRITC-dextran). Emitted fluorescence was split with a 560 nm dichroic. Filter sets used with the Zeiss 7MP setup were bandpass 500–550 nm and bandpass 575–610 nm. A custom microscopy stage reduced image artifacts due to movement and breathing, and allowed repeated positioning.

Images were collected using a 20x, 1.0 NA, apochromatic, 1.7 mm working distance, water immersion objective (Zeiss) on the Zeiss 7MP setup. Fluorescence emission was collected with low-noise, high-sensitivity photomultiplier tubes. The body temperature of the mice was kept constant using a heat pad with a fixed temperature of 32°C. Isoflurane concentration was set between 1–3.0% (in 100% O_2). To visualize cerebral vessels, fluorescent dextran-conjugated tetramethylrhodamine isothiocyanate (**TRITC**; MW = 500,000 $g{\cdot}mol^{-1}$; Sigma) was diluted to 50 $mg{\cdot}ml^{-1}$; 100 μl of this solution was injected retro-orbitally immediately prior to imaging.

For long-term tracking of single DTCs, images were acquired at a wavelength of 750 nm over a region of 420 × 420 μm in one focal plane, at a depth of 400 μm from the brain's surface. Each image stack consisted of 12 to 15 images over 50 μm, taken at an interval of 4 μm every 30 seconds at resolution of 512 × 512 pixels. Multiple image stacks for a selected region were taken. We followed 6 to 12 regions of interest in the cortex where tumor cells were visible over time, imaging at day three post-injection, then every three to four days. If tumor cells disappeared from view in one area, we imaged this area one more time before ceasing to image that position. As described previously by Kienast et al.[14], we were able to re-image the same cells over time using a coordinate chart, as well as using unique vascular patterns and branch points as landmarks.

Immunofluorescent staining.

Fixed mouse brains were flash frozen on dry ice. 30 μm sections were cut on a Leica sliding microtome (Leica Microsystems) and dehydrated overnight in anti-frozen cryostorage solution (PBS with 30% sucrose, 30% ethylene glycol and 1% PVP-40) at −20°C. Free-floating sections were washed twice with PBS to rehydrate, then permeabilized in 10% TritonX-100/PBS for 30 minutes at room temperature. Tissues were blocked for one hour at room temperature in 3% TritonX-100/5% goat serum/PBS. All primary

antibodies (details provided in Reporting Summary) were diluted in a blocking solution of 0.05% TritonX-100/5% goat serum/PBS and added overnight under gentle rocking at room temperature. The following day, slides were washed at least three times in PBS, then counterstained in blocking solution containing 4',6-Diamidine-2'-phenylindole dihydrochloride (**DAPI**; 2 μg/mL), goat anti-chicken AlexaFluor (AF) 488, goat anti-hamster AF568, goat anti-mouse AF647 or goat anti-rabbit AF647, all at 1:500 for 60 minutes at room temperature.. After washing in PBS, sections were mounted on Superfrost Plus slides (VWR) and imaged on a Zeiss LSM 700 confocal microscope using either a 1.1NA 40x water-immersion objective or a 1.4NA 63x oil-immersion objective.

Quantification of vessel coverage.

Four discreet phases of brain metastatic progression were identified: **i**) dormant DTC (1–5 cells, all Ki67$^-$); **ii**) dormant micrometastasis (6–50 cells, Ki67$^-$); **iii**) proliferative micrometastasis (6–50 cells, at least one Ki67$^+$ cell) and **iv**) macrometastasis (>100 cells) as justified previously[65]. For each lesion, the associated vessel was imaged for AQP4 (astrocytes), PDGFRβ (pericytes) or laminin-α2. The Z-stack containing the largest intersection of the DTC-associated vessels was chosen for measurement. The total length of vessel and AQP4, PDGFRβ, or laminin-α2 coverage was measured using the hand tool in Imaris software (Oxford Instruments). Vessel coverage was calculated as the total AQP4, PDGFRβ or laminin-α2 signal converging on the vessel divided by vessel length. This value was multiplied by two to account for both surfaces of the vessel in the two-dimensional representation.

Immunofluorescence quantification.

Laminin-γ1, laminin-α2 and AQP4 coverage was quantified for Nestin-Cre, Lamc1$^{flox/flox}$ conditional knockout mice and their littermate controls using n = 6 sections per mice, n = 3 mice per condition. To quantify total IF intensity, the "Filament" functional module in Imaris was used to mask CD31$^+$ vessels and the intensity sum of laminin-γ1, laminin-α2 and AQP4 staining was measured with the built-in statistic function (Fred Hutch Imaging Core). The vessel coverage was calculated as the ratio of total IF intensity of laminin-γ1, laminin-α2, or AQP4 to CD31. To quantify YAP1 intensity and its nuclear-to-cytoplasmic fraction, the "Surface" functional module in Imaris was used to mask GFP$^+$ tumor cells, defined as DTCs (1–5 cells), micrometastasis (6–50 cells) or macrometastasis (>100 cells). The "Manual Surface Creation" tool was used to draw the contour of cell body (GFP$^+$) and nuclei (DAPI$^+$) of selected tumor cells used method described previously[66]. Total immunofluorescence intensity of YAP1 staining was measured with the built-in statistic function of Imaris software.

Multiplex immunohistochemistry for human specimens.

We analyzed normal human brain tissue and human brain tissue from patients with a history of breast cancer obtained from the University of Washington's Adult Changes in Thought (ACT) study. We also analyzed breast cancer-brain metastases, which we accessed through Northwest Bio Trust. In all cases, samples were de-identified when they were provided to us. We did not have access to any identifying information related to these specimens over the

course of our study. Per Fred Hutchinson Cancer Research Center Institutional review Board guidelines, this was not considered human subjects research.

At Huntsman Cancer Institute, the informed consent process falls under human subjects research, and is approved by the IRB, but tissue collection on the decedents is not considered human subjects research. Detailed patient information is provided in Supplementary Table 1.

mIHC staining.—Formalin-fixed paraffin-embedded tissue slides were baked for one hour at 60°C. The slides were dewaxed and stained on a Leica BOND Rx autostainer (Leica, Buffalo Grove, IL) using Leica Bond reagents for dewaxing (Dewax Solution), antigen retrieval/antibody stripping (Epitope Retrieval Solution 2), and rinsing after each step (Bond Wash Solution). Antigen retrieval and antibody stripping steps were performed at 100°C with all other steps at ambient temperature.

Endogenous peroxidase was blocked with 3% H2O2 for eight minutes followed by protein blocking with TCT buffer (0.05M Tris, 0.15M NaCl, 0.25% Casein, 0.1% Tween 20, pH 7.6) for 30 minutes. The first primary antibody (position 1) was applied for 60 minutes followed by the secondary antibody application for 10 minutes and the application of the tertiary TSA-amplification reagent (PerkinElmer OPAL fluor) for 10 minutes. A high stringency wash was performed after the secondary and tertiary applications using high-salt TBST solution (0.05M Tris, 0.3M NaCl, and 0.1% Tween-20, pH 7.2–7.6). The primary and secondary antibodies were stripped with retrieval solution for 20 minutes before repeating the process with the second primary antibody (position 2) starting with a new application of 3% H2O2. The process was repeated until all six positions were completed; however, there was no stripping step after the final position. Slides were removed from the stainer, stained with DAPI for five minutes, and coverslipped with Prolong Gold Antifade reagent (Invitrogen/Life Technologies, Grand Island, NY). Slides were cured at room temperature. Species-specific Polymer HRP was used for all secondary applications.

mIHC quantification.—Whole slide images were acquired on the Perkin Elmer Polaris Automated Imaging System (Akoya Biosciences, Marlborough, MA) under 20X magnification. Regions of interest were selected for imaging using Phenochart and multispectral image tiles were acquired using the Polaris. Images were spectrally unmixed using Phenoptics inForm software and exported as multi-image TIF files.

Tiles were stitched and analyzed with HALO image analysis software (Indica Labs, Cooales, NM). Cells were identified based on nuclear recognition (DAPI), then fluorescence intensity of the estimated cytoplasmic areas of each cell was measured. A mean intensity threshold above background was used to determine positivity for each fluorochrome within the cytoplasm, defining cells as either positive or negative for each marker. The positive cell data was then used to define colocalized populations.

The HighPlex FL function was applied to calculate laminin-α2 coverage on vessel. A tissue classifier was trained to recognize Her2/CK7^{+} tumors, CD31^{+} vessels and laminin-α2^{+} endfeet based on defined cell type morphology and average intensity of cell marker staining. To quantify laminin-α2 vessel coverage, the total length of the vessel and laminin-

α2 coverage was measured using the hand tool in HALO and the sum of laminin-α2 convergence on vessel area was divided by vessel length (x2). For brain metastases and normal brain samples, 2–3 sections from each patient were used and 50 classified vessel units from each sample were analyzed. For rapid autopsy samples of tumor uninvolved brain, four micrometastases were identified and analyzed.

Experiments testing the impact of loss of laminin-211 on DTC dormancy in immune competent mice.

To generate the Nestin-Cre/laminin-γ1 knockout (N-γ1-KO) mice, homozygous floxed laminin-γ1 ($Lamc1^{flox/flox}$) mice on a C57BL/6 background were crossed with nestin-Cre transgenic mice. The double heterozygous $Lamc1^{flox/+;}$ nestin-Cre/+ mice were crossed with homozygous $Lamc1^{flox/flox}$ mice to obtain mice that were homozygous for the floxed laminin-γ1 allele and also carried the Cre transgene. To generate immune tolerance to tdTomato, the N-γ1-KO mice were further crossed with Cx3cr1-GFP;CCR2-RFP reporter mice[61]. Littermates that were homozygous for the floxed laminin-γ1 allele but did not carry the Cre transgenes or were heterozygous for the floxed laminin-γ1 allele and also carried the Cre transgenes were used as controls in all experiments. For the metastasis assay, only heterozygous CCR2-RFP mice were used. 1×10^5 brain tropic tdTomato-E0771 mammary tumour cells that we had passaged through mice five-times to enrich for brain metastatic capacity were delivered into immune-competent, N-γ1-KOs or control littermates by ultrasound-guided intracardiac injection. Mice were sacrificed 13 days later due to neurological symptoms that developed in the N-γ1-KO group.

Quantification of brain metastatic lesion area.—Thirteen days after intracardiac injection, mice were euthanized and the brains processed for sectioning and staining as described above. An array of 20–25 brain sections was arranged to cover a slide (VWR Superfrost Plus Microslide) which was tilescanned completely using a Zeiss LSM 700 confocal microscope with 0.3 NA 10x air objective. $TdTomato^+$-positive DTCs were thresholded to remove all background and create a binary image in Imaris software. $TdTomato^+$ brain lesions were masked using the “Surface” functional module and lesions ≥ 25000 μm^2 in diameter were quantified with the built-in statistic function. Brain sections from uninoculated mice that had undergone the entire staining protocol were used as a negative control.

Ovary metastasis measurements.—Metastatic lesions on ovaries were confirmed by *ex vivo* imaging with an Axiozoom fluorescent stereoscope. The area (S) of ovary lesions was measured in ImageJ using the measurement analyze function. 3D volume was calculated using the equation V= 1330*S*SQRT(S/π).

Single cell transcriptomics of brain metastases and micrometastases.

Sample collection and digestion for single cell RNAseq.—TdTomato-mVenus-$p27K^-$ T4-2 breast cancer cells (5×10^5 cells in 100 μl PBS) were injected via ultrasound-guided injection into the left ventricle of six to eight week old female NOD SCID mice (n = 4). Animals were euthanized one month post-injection and perfused with 25 mL cold DEPC-treated PBS (Sigma) via the left ventricle. The brain was removed and placed

in ice cold Hank's Balanced Salt Solution (HBSS) in a 10 cm dish. Fresh brain tissues were dissected under an Axiozoom fluorescent stereoscope (Zeiss) to distinguish tdTomato$^+$ metastatic lesions from grossly uninvolved brain. The metastatic and uninvolved brain tissue were separated and minced using a razor blade, then enzymatically dissociated with papain (2 mg/ml) (Worthington Biochemical Corporation) and 0.06 mg/ml DNase I (Worthington Biochemical Corporation) in HBSS. A single cell suspension was obtained by incubating samples at 37 °C for 30 minutes with agitation every five minutes.

Flow sorting of tdTomato$^+$ DTCs from metastatic lesions vs uninvolved brain.—Single cell suspensions were analyzed and sorted on a BD FACSymphony flow cytometer (BD Biosciences, Fred Hutch Flow Cytometry core). 1 μg/ml DAPI was added to the cell suspension five minutes before sorting as a viability dye. Analyses were gated off forward and side scatter and singlets. Dead cells were excluded by positive DAPI signal. Live cells were further gated off PE-Texas Red (for tdTomato) and FITC-A (for mVenus-p27). Non-inoculated brain cell suspension and tdTomato- or mVenus-p27-expressing T4-2s were used to set gates.

TdTomato$^+$ populations were collected from both uninvolved and macrometastatic tissue, pooled from four mice, to make the following comparison: for uninvolved brain, mVenus-p27$^+$ (52 cells) versus mVenus-p27$^-$ (4,387 cells); and for macrometastatic lesions, mVenus-p27$^+$ (926 cells) versus mVenus-p27$^-$ (92,433 cells). The unexpectedly low count of mVenus-p27$^+$ DTCs from uninvolved brain (due to weak mVenus expression compared to background signal in brain) necessitated combining it with the mVenus-p27$^-$ population to bring the uninvolved brain sample to 4,439 cells total and relabeled as "Micrometastases". These DTCs together with 926 mVenus-p27$^+$ and 10,000 mVenus-p27$^-$ cells from metastatic lesions (together labeled as "Metastases") were processed for single cell RNA sequencing.

Single cell capture, library preparation, and sequencing.—Single-cell libraries were prepared using the Chromium 3′ v2 platform (10X Genomics) following the manufacturer's protocol[67]. Briefly, single cells were partitioned into gel beads in emulsion in the 10X Chromium Controller instrument followed by cell lysis and barcoded reverse transcription of RNA, amplification, shearing and 5′ adapter and sample index attachment. Cells from the three groups indicated above were loaded separately onto the Chromium Chip A for indexing before libraries were combined for paired-end sequencing on the Illumina HiSeq2500 (PE1 54 bp and PE2 66 bp). The mixed libraries were sequenced on one HiSeq lane, at an initial depth of approximately 150 million reads.

The number of reads that provided meaningful information was calculated as the product of four metrics: (1) valid barcodes; (2) valid UMI; (3) associated with a cell barcode; and (4) confidently mapped to exons. After quality control, 1,779 micromet-derived DTCs were recovered, with 52,840 mean reads per cell and 919 median genes per cells. 4,032 mVenus-p27$^-$ cells were recovered from metastatic lesions, with 22,425 mean reads per cell and 2,716 median genes per cells. 251 mVenus-p27$^+$ (quiescent) cells were recovered from metastatic lesions, with 429,394 mean reads per cell and 4,585 median genes per cells.

Single cell RNAseq data preprocessing.—The resulting count tables from Cellranger were post-processed using Scanpy (v1.7.0)[68]. First, cells were filtered for standard quality control metrics with the following thresholds: ⩾ 400 unique genes, < 4500 unique genes, ⩾ 700 UMI, < 30,000 UMI, and < 10% of total UMIs mapping to mitochondrially-encoded genes. The counts were then normalized to 10,000 total counts per cell and log transformed. Principle components were calculated (n=50), a nearest neighbor graph (k=30) was calculated using the principle component space, and Leiden clustering was performed on the resulting graph with a resolution of 0.8, ultimately resulting in 10 total clusters. The UMAP embedding was calculated using the self-assembling manifold method[69] with k=30 and a Euclidean distance metric. Differential gene expression analysis among clusters was performed using the Scanpy rank_genes_groups function (Wilcoxon method). For each cluster, genes from the differential expression analysis were filtered to have Score > 0, log fold change ⩾ 0.5, FDR ⩽ 0.05, and percent non-zero expression within the respective cluster ⩾ 10%. The resulting genes for each cluster were then input to string-db with the following parameters: highest confidence interactors (probability scores > 0.9), 20 interactors in the first shell, no interactors in the second shell. The graph was then analyzed for pathway enrichment using the KEGG database, and the top 5 pathways (ranked by lowest FDR) with FDR ⩽ 0.05 were retained in the bar graphs. The YAP target gene signature was obtained from Wang *et al*[48]. The S and G2/M phase signature genes were obtained from Satija *et al*[70]. The cellular quiescence gene signature was obtained from Cheung and Rando[49]. All gene signature scores were calculated using the Scanpy score_genes function using default parameters. Correlations between YAP target gene score and each signature score were obtained using the scipy (v1.6.0) spearmanr function. All custom plots were rendered using standard plotting utilities in python: matplotlib (v 3.3.4), seaborn (v 0.11.1), and scanpy (v1.7.0).

Cell culture and reagents.

Freshly isolated human umbilical vein endothelial cells (**HUVECs**) were provided kindly by Dr. Andrew Putnam (University of Michigan) and propagated in fully supplemented EGM-2 growth medium (Lonza). Human hepatic sinusoidal endothelial cells (**HHSEC**, ScienCell#5000) were cultured in EGM-2 (Lonza). Human brain vascular adventitial fibroblasts (**HBVAFs**, #1110) and human lung fibroblast (**LFs**,#3300) were obtained commercially (ScienCell) and propagated in high-glucose DMEM supplemented with 10% fetal bovine serum (FBS, ThermoFisher). Human astrocytes (ScienCell#1800) were cultured in Astrocyte Growth Media (Lonza). Bone marrow-derived human mesenchymal stem cells (**MSCs**, ScienCell#7500) were cultured and propagated in low-glucose DMEM supplemented with 10% FBS. All primary human cells were used in experiments from passages eight to ten.

T4-2 cells were kind gift of Dr. Mina Bissell at Lawrence Berkeley National Laboratory, University of California, Berkeley, and grown as described previously[62]. MDA-MB-231 were purchased from ATCC (#HTB26) and its brain-metastatic derivative line MDA-MB-231-BR7 was generously provided by Dr. Patricia Steeg (NCI) [64]. Both MDA-MB-231 and MDA-MB-231-BR7 cells were grown in high-glucose DMEM supplemented with 10%

FBS. Triple-negative murine mammary tumor line E0771 (Ch3 Biosystems#94A001) were grown in high-glucose DMEM supplemented with 10% FBS.

Generation of lung, bone marrow and liver microvascular niches.—Lung and bone marrow microvascular niche (**MVN**) cultures were generated as previously described[11]. Liver MVN cultures were generated by seeding 5×10^4 hepatic stellate cells alone or with 1×10^4 mCherry-HHSEC in 100 μl EGM-2 in 96-well culture plates. Plates were left undisturbed on a flat surface for 20 minutes to allow cells to settle evenly prior to incubation. Media (100 μL EGM-2/well) was changed every 72 hours.

Generation of brain MVNs.—1×10^5 HBVAFs were seeded alone or in combination with 1×10^4 mCherry-E4Orf1-HUVEC and/or 1×10^4 human astrocytes. Cells were suspended in 100 μl EGM-2 per well of a 96-well culture plate. Plates were left undisturbed on a flat surface for 20 minutes to allow cells to settle evenly prior to incubation in lower oxygen conditions (16% O_2 and 5% CO_2).

After 10 days, 100 YFP-expressing tumor cells in 100 μl unsupplemented DMEM/F12 were seeded on each well after washing cultures three times with PBS. Cells were allowed to settle undisturbed for 15–25 minutes at room temperature before being returned to an oxygen-controlled environment. One day later, cultures were imaged on a Zeiss LSM700 confocal microscope using a 0.3 NA 10X air objective. The objective was centered in each well before acquisition of a 6×6 tilescan at 512 × 512 pixel resolution (zoom = 0.7) that captured the near-entirety of each well. Cultures were maintained with media changes every 72 hours and imaged again at day 10.

Add-back experiments with purified laminins.—Laminin-211 (Merosin, Sigma), −111, −411 or −511 (Biolamina), were dialyzed twice in cold PBS (1 ml laminin/2 L PBS) at 4°C overnight to remove all carrier agents. The dialyzed solution was filtered (0.2 μm) and protein concentration was determined using a DC protein assay kit (Pierce) following manufacture instructions. Stocks were generated at 1 mg/ml and diluted to 0.1 μg/ml, 1 μg/ml, 2 μg/ml, 5 μg/ml and 10 μg/ml in DMEM/F12. Cultures were treated immediately after seeding tumor cells and refreshed every two days. PBS was used as a vehicle control.

Conditioned medium experiments.—1×10^5 HBVAFs were seeded alone or in combination with 1×10^4 mCherry-E4Orf1-HUVEC and 1×10^4 human astrocytes. After 10 days of vasculature network formation, each well was washed three times with PBS and replaced with 100 μl unsupplemented DMEM/F12. Thirty-six hours later, conditioned media from the fibroblast and MVN co-cultures were collected and spun down at maximum speed for five minutes to remove cell debris, then filtered (0.2μm), aliquoted and stored at −80°C. Cultures were treated with conditioned media immediately after seeding tumor cells and refreshed every other day. Conditioned media was mixed 1:1 with fresh DMEM/F12 medium before use. DMEM/F12 served as a vehicle control.

ECM overexpression experiments.—Open reading frame (**ORF**) constructs for vitronectin (VTN), lumican (LUM), secreted protein acidic and rich in cysteine (SPARC), galectin-1 (LGALS1), type I collagen A1 chain (COL1A1), annexin A2 (ANXA2), and

versican (VCAN) in the pLX304-CMV-V5 tag-ORF backbone were obtained from the Paddison laboratory (Fred Hutch)[71]. Type V Collagen (Col5A2), type VI collagen (Col6A2), elastin microfibril interface-located protein 1 (EMILIN1), decorin (DCN), spondin 2 (SPON2), thrombospondin 1 (TSP1), EGF containing fibulin extracellular matrix protein 2 (EFEMP2), and type I collagen A2 chain (COL1A2) were cloned into the pLX304-CMV-V5 tag-ORF backbone by Gibson assembly using cDNA amplified from total RNA extracted from brain MVNs via Qiagen RNeasy Mini Kit. Type XVIII Collagen (COL18A1), agrin, and laminin-α2 (LAMA2) in the pLX304-CMV-V5 tag-ORF were custom ordered from VectorBuilder.

HBVAFs were transduced with pLX304-CMV-V5 tag lentivirus encoding the 18 ECM molecule ORFs listed above, or empty vector as the control. Lentivirus was used at MOI of 5 for smaller proteins and MOI of 10 for larger proteins including VCAN, COL18A1, agrin, and LAMA2. Infected HBVAFs were selected for four days in 10 μg/ml blasticidin (Sigma), expanded, and stored in liquid nitrogen until experiments.

Immunofluorescent staining of MVNs and Quantification of tumor cell growth and proliferative status in MVNs were essentially performed as already described[11].

Knockdown, knockout and overexpression constructs.

Generation of pLenti-CMV-YFP and retroviral pBMN-mCherry were previously described[11]. pCDH-CMV-MCS-EF1a-eGFP-T2A-Puro (System Bioscience #CD510B-1) was a kind gift from Dr. Weilin Jin (Shanghai Jiao Tong University, China). To generate the pLVX-tdTomato-IRES-Hygro construct, tdTomato cDNA was isolated from the pQC-membrane tdTomato IX construct (Addgene #37351) by polymerase chain reaction (PCR) and subcloned into the pLVX-IRES-Hyg vector (Clontech #632185). pLenti-VIIb-EVP-Neo-mVenus-p27K$^-$ was generously provided by the Paddison laboratory (FHCRC). This vector encodes a mutant form of p27 that lacks cyclin-dependent kinase inhibitory activity, and an mVenus reporter for quiescence[72]. pBABE-YAP1-S127A, S127AS397A and S94A mutant constructs[73] were kind gifts from the Vasioukhin lab (FHCRC). YAP mutant cDNA regions were amplified and subcloned into the pCDH-CMV-MCS-EF1a-eGFP-T2A-Puro construct with a FLAG tag at the 5’ end. Stable knockdown of human DAG1 was achieved with shRNAs cloned with a mir30 background in the pGIPZ vector (Dharmacon). To target human ITGA6, ITGB1, YAP1 or murine DAG1, the pLKO.1-blast shRNA plasmid (Addgene#26655) was used. All shRNA sequences are detailed in Supplementary Table 3.

Co-immunoprecipitation and Western blotting.

MDA-MB-231 cells were lentivirally-transduced to overexpress FLAG-tagged YAP1. Stable cell lines were established and cultured on 100 cm dishes coated with collagen (Purecol, Advanced Biomatrix) or human merosin (Sigma, CC085) mixed with 0.01% poly-L-lysine (Sigma). Two to three days later when dishes reached 60% confluence, cells were lysed with modified radioimmunoprecipitation assay (RIPA) lysis buffer (50 mM Tris-HCl, pH 7.4, 50 mM NaCl, 1 mM EDTA, 0.2% sodium deoxycholate, 0.05% sodium dodecyl sulfate , 0.2% Triton X-100, 0.5% NP-40 [IGEPAL]) supplemented with complete protease and phosphatase inhibitors (Roche). Samples were centrifuged at 15,000 x *g* for 15 minutes at 4

°C, then ~1 mg of supernatant per sample was immunoprecipitated with anti-DYKDDDDK FLAG Tag (L5) Affinity Gel (Biolegend, 651501) or control rat IgG agarose (Rockland, 012–0050), at 4°C overnight. The beads were washed 3 times in fresh RIPA buffer and the precipitated protein complex was eluted by boiling samples in 2X Laemmli sample buffer with 10% β-mercaptoethanol for five minutes. Five percent of total protein extract was used as loading input for immunoprecipitation. The presence of immunocomplexes were detected by standard Western blot and develop using Li-Cor Odyssey. Densitometry was performed on Odyssey software v3.0. Further information on antibodies used for these studies can be found in the Nature Research Reporting Summary linked to this article.

Proximity ligation assay.

The *in situ* proximity ligation assay (PLA) was conducted using a Duolink™ *In Situ* Red Starter Kit Mouse/Rabbit (Sigma) following the manufacturer's protocol. Free-floating brain sections taken from NOD-SCID mice inoculated with eGFP-T4-2 tumour cells were washed twice with 1x PBS to rehydrate the sections, then permeabilised in 10% Triton X-100/PBS for 30 minutes at room temperature. Tissues were blocked for one hour at 37°C using Duolink Blocking Solution, followed by incubation with either a single antibody (controls) or with both antibodies, diluted in Duolink Antibody Diluent at 4°C overnight. The following primary antibodies were used: rabbit anti-YAP (Abcam, ab205270, 1:300) and mouse anti-β-DAG (Biolegend, 850202, 1:100). The following day, slides were washed at least three times in Duolink Washing Buffer A and incubated with oligonucleotide-conjugated secondary antibodies (PLA Probes) PLUS and MINUS for 60 min at 37°C. Subsequently, sections were washed and incubated with a ligation mixture for 30 min at 37°C, followed by washing and incubating with an amplification mixture (Detection Reagent Red) for 100 min at 37°C. After amplification, the sections were washed and rinsed in 1x and 0.01x Washing Buffer B before mounting the slides using Duolink Mounting Medium with DAPI. Images were acquired with a Zeiss LSM 700 confocal microscope using a 1.1NA 40x water-immersion objective.

Analysis of bone marrow, lung, liver and brain stroma and MVNs via LC-MS/MS.

Bone marrow and lung MVN cultures were established for 12 days in EGM-2, and liver and brain MVN cultures were established for 17 days in EGM-2. Cultures were washed extensively with PBS to remove medium, carefully collected using a p10 pipette tip into 1.5 ml Eppendorf tubes, and flash frozen on dry ice prior to storage at −80°C. Sample digestion, LC-MS/MS analysis, database searching, and protein identification were carried out as previously described[12].

Statistics and reproducibility.

Data were analyzed with GraphPad Prism 9 software or Scanpy (v1.7.0). Statistical significance was determined by unpaired or paired two-tailed Student's t-test (with unequal variations if an F test ruled out the equal variation assumption), one-way ANOVA with Tukey's post hoc test or Dunnett's multiple comparisons test, two-tailed Spearman rank correlation, two-sided Wilcoxon rank sum test, as appropriate for the dataset. Statistical details (for example, sample size and specific test performed) for each experiment are noted in the figure and corresponding figure caption. Data are generally expressed as

mean ± s.e.m., as noted in the figure captions. A P-value < 0.05 was considered statistically significant.

Experiments presented in Fig.3g and Extended Data Fig. 3g were conducted with two biological replicates. All the other experiments were conducted at least three independent times, at minimum in technical triplicate. All experiments were reproducible. For animal experiments, a pilot experiment with 3 animals in each group were conducted for the shDAG1 knockdown experiment showed in Fig. 5g; sample size of the full experiment was then determined using a sample size calculator with power of 80%. Cohort sizes for all other animal experiments were determined based either on power calculations for the experiments displayed in in Fig. 5g and/or on prior experience with metastatic animal model effect sizes[17, 74]. Littermate controls were used for experiments shown in Figure 4. Littermates with or without Lamc1 knockout were housed in same cage upon tumor cell injection; researchers were blinded to the genotype of the animals at this point. No other experiments were randomized. For the experiments using gene modified tumour cells with either overexpression vectors or shRNA knockdown, animals were allocated for injection with control or gene modified tumor cells in repetitive sequence. Upon termination of these experiments, collection and analysis of data were not performed in blinded fashion, due principally to personnel limitations. Across all studies, no datapoints were excluded.

Reporting Summary.

Further information on research design is available in the Nature Research Reporting Summary linked to this article.

Data Availability.

Single cell RNA–sequencing data that support the findings of this study have been deposited in the Gene Expression Omnibus (GEO) under accession code GSE152818. Source data for Figs. 1–5 and 7 and Extended Data Figs. 2-8 have been provided as Source Data files. All other data supporting the findings of this study are available from the corresponding authors on request.

Extended Data

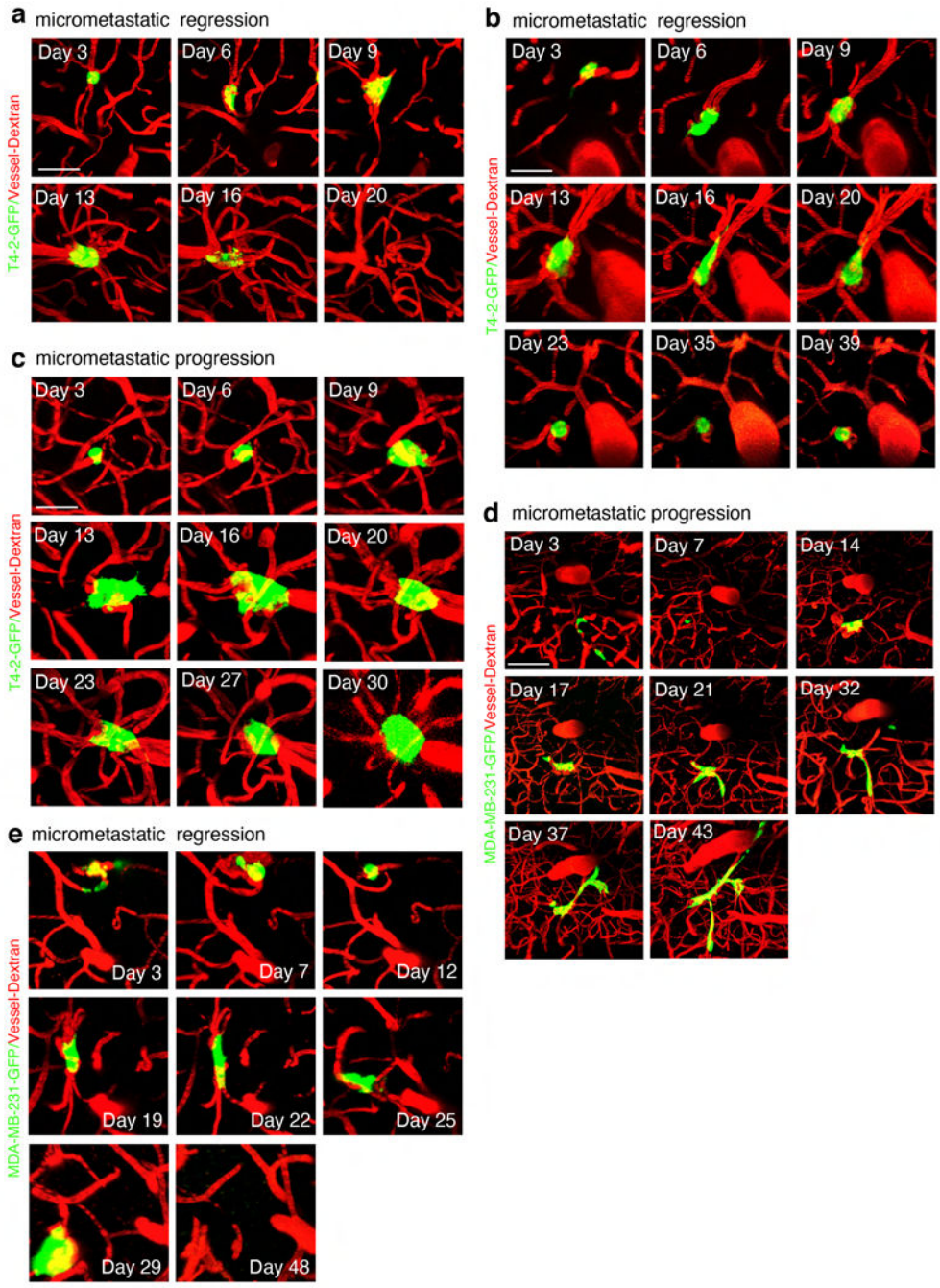

Extended Data Figure 1: Intravital imaging reveals micrometastatic progression and regression of DTCs in brain.

Serial intravital imaging revealed several potential fates for eGFP-T4-2 breast cancer DTCs which reached the brain: **a**) DTCs progress to micrometastatic lesions but regress and die by day 20 post-intracardiac inoculation; **b**) proliferate then regress by day 23, but continue to persist as a single cell through day 39; and **c**) steadily progress to form stable micrometastases. These behaviors were also observed in a second model using MDA-

MB-231 cells: **d**) steady progression to form micrometastases by day 14, which continue to grow along vasculature through day 43; **e**) death/disappearance of micrometastasis by day 29. Representative images of n=16 cells over 6 mice (T4-2) and n=17 cells over 5 mice (MDA-MB-231) over the course of 4 to 7 weeks post-injection were tracked for regression (a,b,e) or progression (c,d). Scale bar = 40 μm.

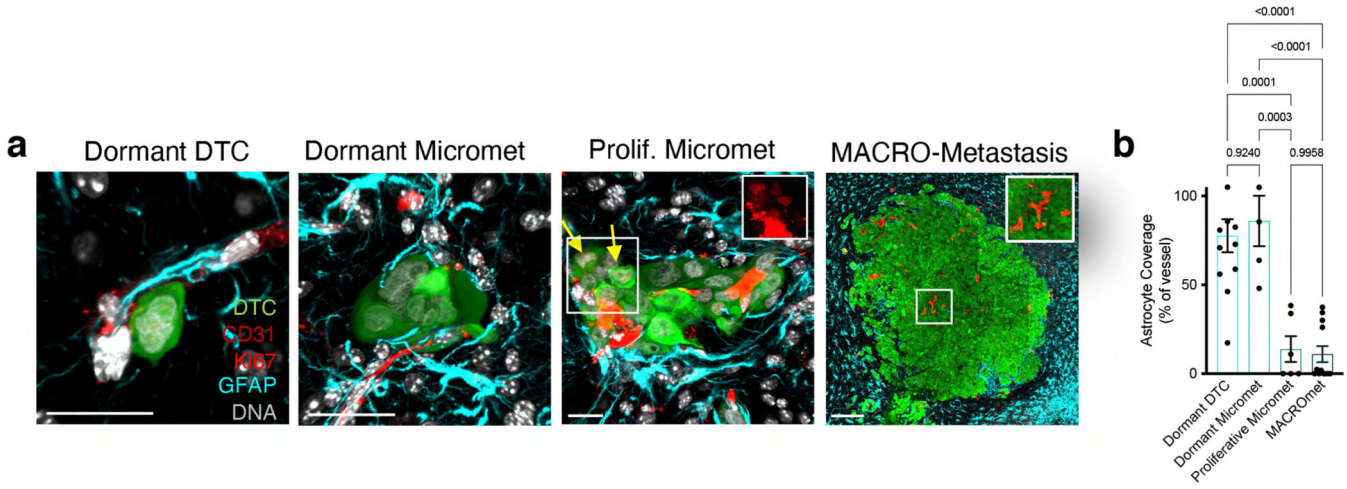

Extended Data Figure 2: GFAP staining confirms that astrocytes are stripped from vessels upon activation of micrometastases.

a) Representative Z-projections of disseminated eGFP-T4-2 cells and astrocyte (GFAP+, cyan) coverage of DTC-associated vessels in the brains of NOD SCID mice across four stages of brain metastatic progression, 8 weeks following intracardiac inoculation. Yellow arrows indicate Ki67+ tumour cells (see inset for CD31 and GFAP channels only). Scale bar = 20 μm. From left to right, images are representative of n = 12, 5, 6 and 12 independent lesions imaged across n=3 mice. **b**) Quantification of astrocyte vessel coverage across metastatic progression. P-values calculated for n=35 lesions across 3 mice by one-way ANOVA and Turkey's post hoc test. Centre line represents the mean, and error bars the s.e.m.

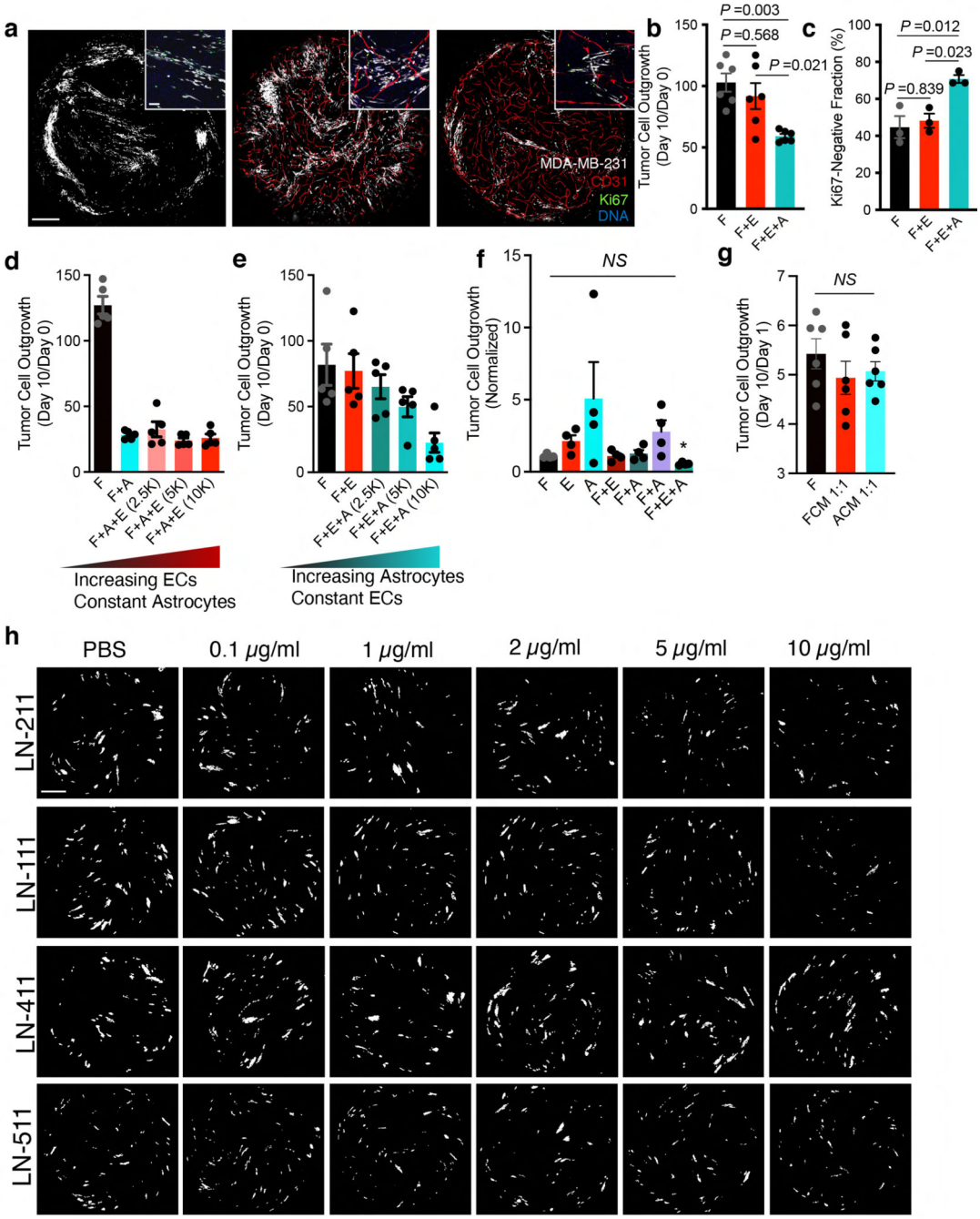

Extended Data Figure 3: Astrocytes suppress breast tumour cell outgrowth in a model of the brain's perivascular niche.

a) Representative IF images of MDA-MB-231 cell outgrowth on F vs. F+E vs. F+E+A co-cultures 10 days post-seeding. Scale bar = 500 μm. Inset: Enlarged images to illustrate Ki67 status of MDA-MB-231 cells. Scale bar = 100 μm. Images representative of 5 wells scanned per condition across n=4 biologically independent experiments. **b**) Tumour cell area fraction of YFP-MDA-MB-231 cells at day 10, normalized by tumour area fraction post-seeding, then normalized to the mean of HBAF (F) condition replicates to correct for the variations

between independent replicates. *P=0.026, **P = 0.003 for n=6 co-culture wells analyzed per condition over 4 independent experiments, by one-way ANOVA and Tukey's post hoc test. **c**) Fraction of Ki67-negative tumour cell clusters. *P=0.012 for F+E+A vs. F; P=0.023 for F+E vs. F+E+A, for n = 6 wells of co-cultures analyzed per condition, 4 independent experiments, by one-way ANOVA and Tukey's post hoc test. **d**, **e**) Tumour cell area fraction of YFP-T4-2 cells at day 10, normalized by tumour area fraction post-seeding, as a function of (**d**) increasing endothelial cell (**EC**) seeding density (while holding astrocyte number constant) or (**e**) increasing astrocyte seeding density (while holding EC number constant). Representative data from one experiment with n = 5 technical replicates, experiments were conducted twice with similar results. **f**) Quantification of normalized tumour area fraction of YFP-T4-2 cells outgrowth on HBAF (F), endothelia (E), astrocyte (A), all pairwise combinations, and F+E+A co-cultures, 10-days after seeding. NS denotes no significance (P>0.37); *P<0.05 compared to F condition, for n = 5 sets of co-cultures analyzed per condition over 4 independent experiments, by one-way ANOVA and Tukey's post hoc test. **g**) Normalized tumour area fraction 10 days after addition of conditioned media diluted 1:1 with fresh medium. NS denotes no significance (P>0.47), for n = 6 wells per co-culture condition, analyzed for two independent experiments by one-way ANOVA and Tukey's post hoc test. **h**) Representative 96-well tile scans of YFP-T4-2 cells grown on HBAF, in the presence of indicated concentrations of Laminin (LN)-211, LN-111, LN-411 or LN-511, 10 days post-seeding. Images are representative of n=5 sets of co-cultures analyzed per condition across n=3 biologically independent experiments. Scale bar = 1 mm. All data are presented as mean values +/− SEM..

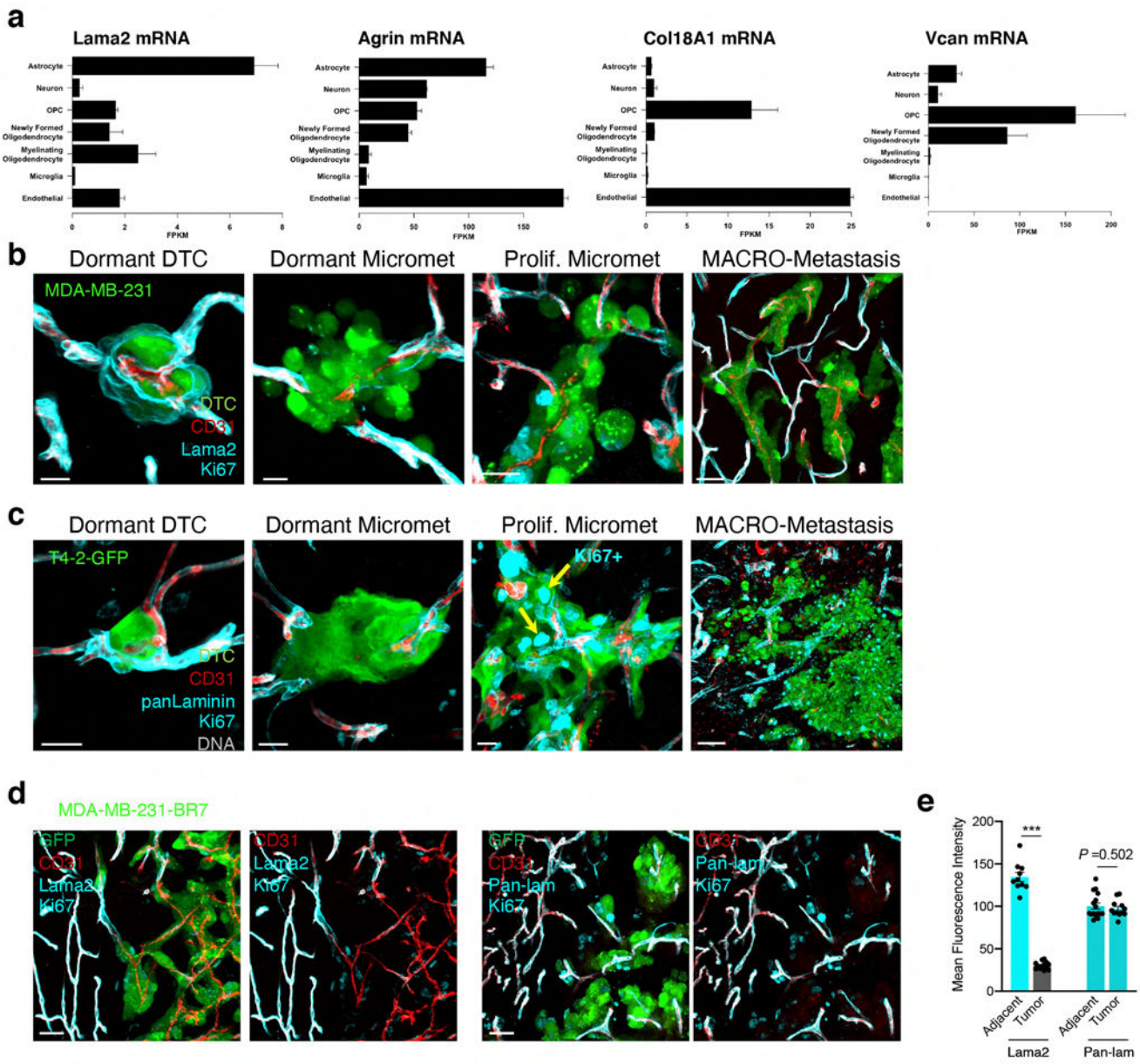

Extended Data Fig. 4: Lama2 is predominantly expressed by astrocytes, and is stripped from vessels over the course of metastatic progression.

a) Transcript expression levels for Lama2, Agrin, Col18A1, and Vcan for astrocytes, neurons, oligodendrocyte progenitor cells (OPC), newly formed oligodendrocytes, myelinating oligodendrocytes, microglia and endothelial cells, immunopanned from adult murine brains and sequenced by RNAseq. Data are reported as FPKM, and were generated by querying brainrnaseq.org. **b, c**) Representative Z-projections of disseminated (b) mCherry-MDA-MB-231 cells (false colored green for consistency) or (c) eGFP-T4-2 cells in brains of NOD-SCID mice ~8 weeks after intracardiac inoculation, demonstrating that stripping of (**b**) Laminin-α2 but not of (**c**) other laminins coincides with metastatic progression. Arrows indicate Ki67+ nuclei in a micrometastatic cluster. Scale bar = 20 μm for three leftmost panels and 100 μm for MACRO-Metastasis. Images representative

of n = 6 sections per mouse acquired for n=3 mice per condition. **d**) Representative IF staining for Laminin-α2 (left panels) and pan-laminin (right panels) to assess vessel coverage in brain-tropic MDA-MB-231-BR7-derived metastatic lesions. Scale bar = 20 μm. From left to right, images representative of n = 13, 10, 12 and 16 independent fields obtained across n=4 mice. **e**) Mean fluorescent intensity of Laminin-α2 and pan-laminin within macrometastatic lesions (“Tumour”) and lesion-adjacent regions (“Adjacent”). ***P < 0.0001 when comparing tumour to adjacent tissue, for n = 51 total lesions across 4 mice by unpaired, two-tailed t-test. Data are presented as mean values +/− SEM.

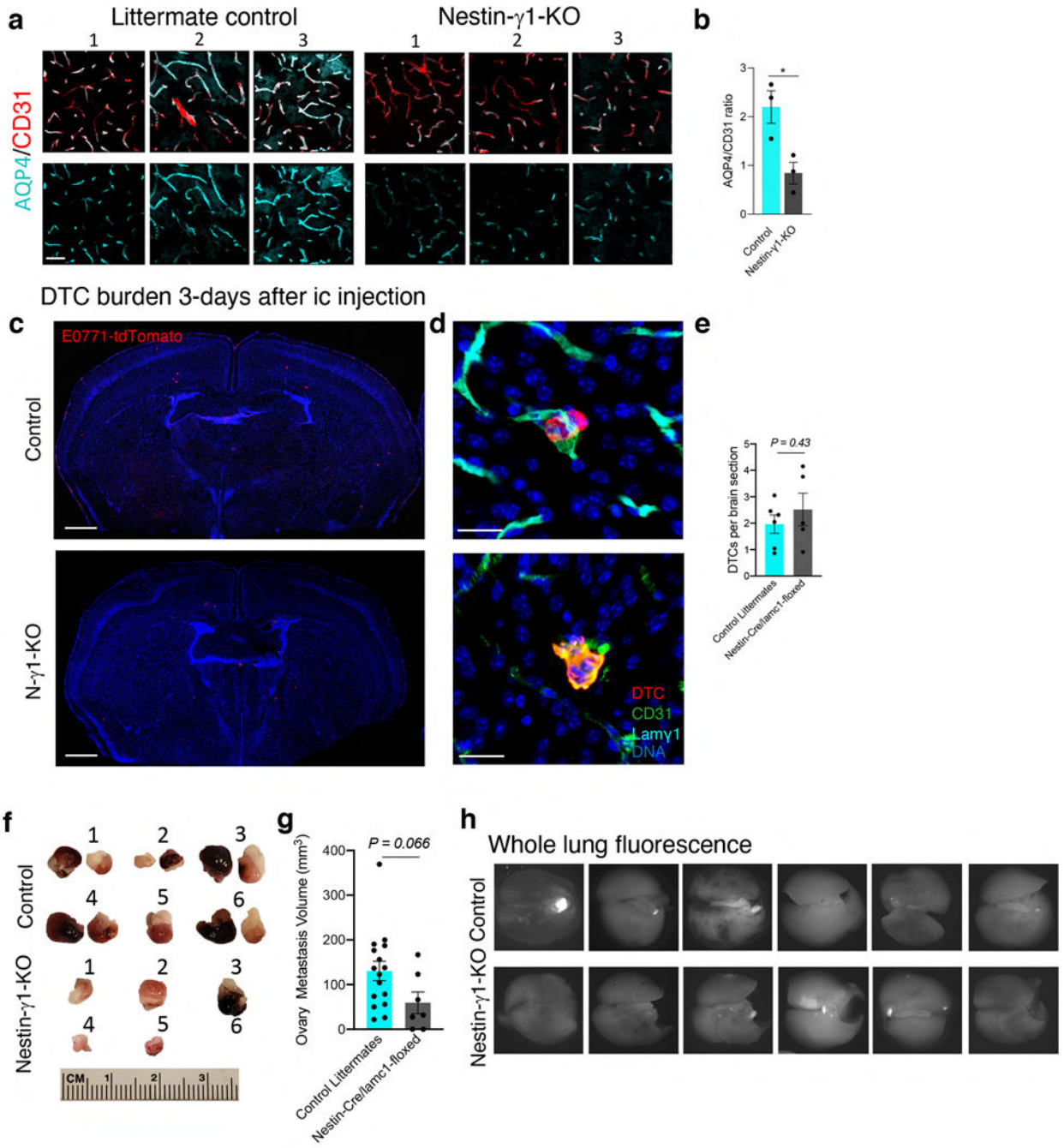

Extended Data Fig. 5: Further characterization of Nestin-drive KO of lamc1.

a) Representative IF staining of AQP4 and CD31 from Nestin-Cre, Lamγ1flox/flox conditional knockout (N-γ1-KO) mice and littermate controls. Samples from 3 different mice shown. Scale bar = 30 μm. n = 6 sections/mouse were analyzed for n=3 mice per condition. **b**) Quantification of AQP4 vessel coverage for control and N-γ1-KO mice. *P=0.028 for 6 sections analyzed per mouse, averaged across n=3 mice per condition, by unpaired, two-tailed t-test. **c**) Tilescan of one coronal section of the brain 3 days after intracardiac delivery of tdTomato-E0771 to either N-γ1-KO mice or control littermates.

Scale bar = 1 mm. **d**) Enlarged representative images of extravasated DTCs from the tilescans in (**c**). Scale bar = 20 μm. **e**) Quantification of extravasated single tdTomato-E0771 DTCs or clusters per brain section in control and N-γ1-KO mice. P = 0.43 for n=6 control mice and n= 5 N-γ1-KO mice, by two-tailed t-test. **f**) Representative bright field images of whole ovary metastases from N-γ1-KO mice or control littermates following intracardiac injection of tdTomato-E0771 cells. Ruler shown for scale. **g**) Quantification of volume of ovary metastases in control and N-γ1-KO mice. P = 0.066, for n = 9 control littermates and n = 7 N-γ1-KO mice, by two-tailed t test. Metastases from both ovaries were counted. **h**) Representative fluorescent images of the whole lung of N-γ1-KO mice or their control littermates following inoculation with tdTomato-E0771 cells, 13 days post-intracardiac injection. Tumour lesions are in white. n=6 mice for both N-γ1-KO and control littermates groups. Data are presented as mean values +/− SEM.

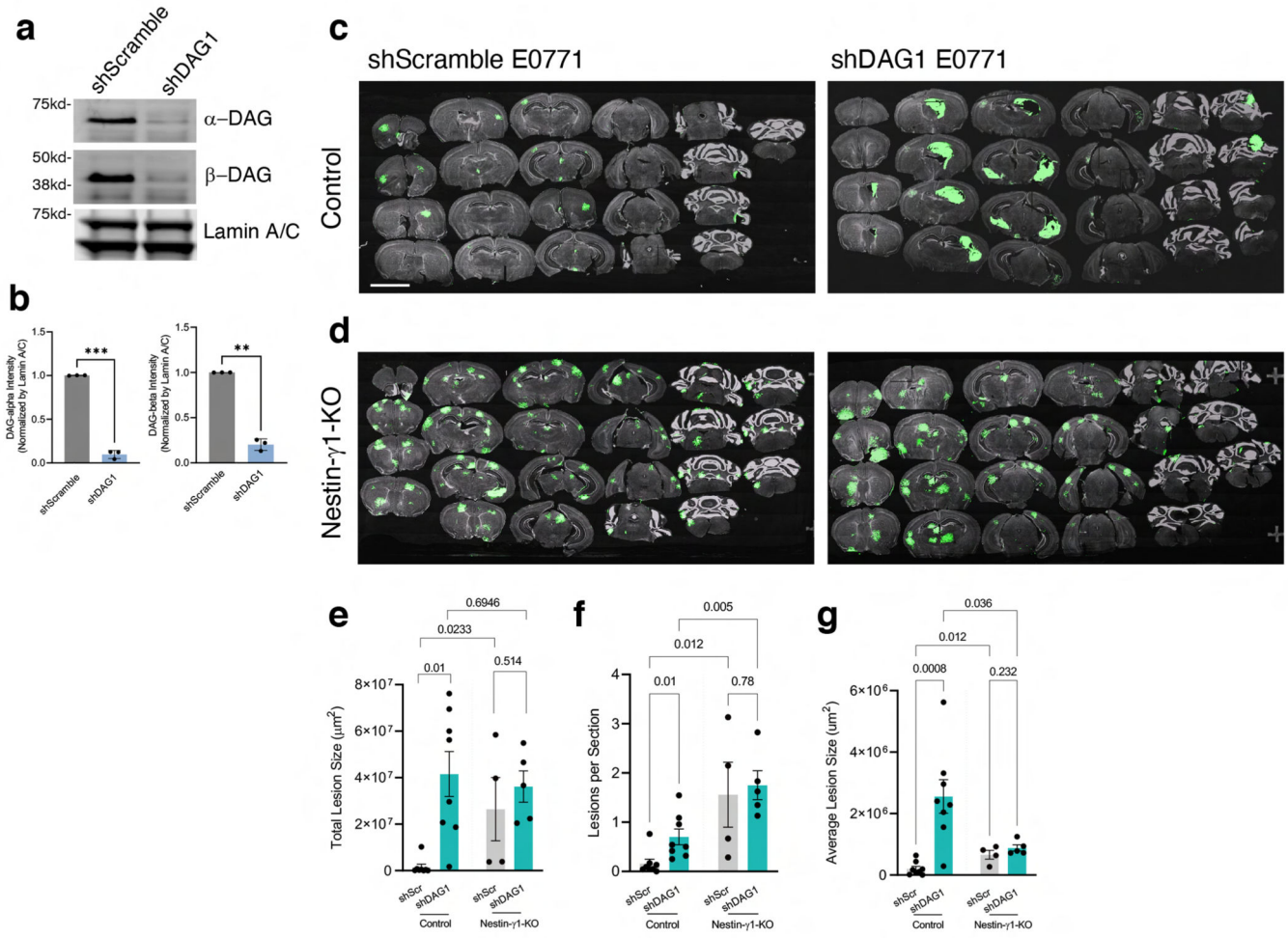

Extended Data Fig. 6: Knockdown of DTC dystroglycan promotes metastatic progression of E0771 hosts; this effect is saturated in N-γ1-KO mice.

a) Representative immunoblot of E0771 cells infected with non-targeting shRNA (shScramble) or shDAG1. Blot was co-stained for α-DAG, β-DAG and Lamin A/C as a loading control. Blots representative of n=3 biologically independent experiments. **b**)

Integrated intensity of α-DAG and β-DAG, normalized to their respective loading control (Lamin A/C) and subsequently to shScramble band on each blot. **P=0.002 , ***P= 0.0009 for n=3 biologically independent experiments, calculated by paired two-tailed t-test. **c**, **d**) Representative immunostains of brain sections (20–25 sections/brain) from (**c**) control littermates or (**d**) N-γ1-KO mice and, 13 days after intracardiac inoculation with either shScramble (left panels) or shDAG1 (right panels) tdTom-E0771 tumour cells. Scale bar = 5 mm. Quantification of (**e**) total lesion size, (**f**) number of lesions per section, and (**g**) average lesion size in these mice. P-values for n=8 control mice per group or n = 4 N-γ1-KO mice per group calculated by two-tailed t-test. Data are presented as mean values +/− SEM.

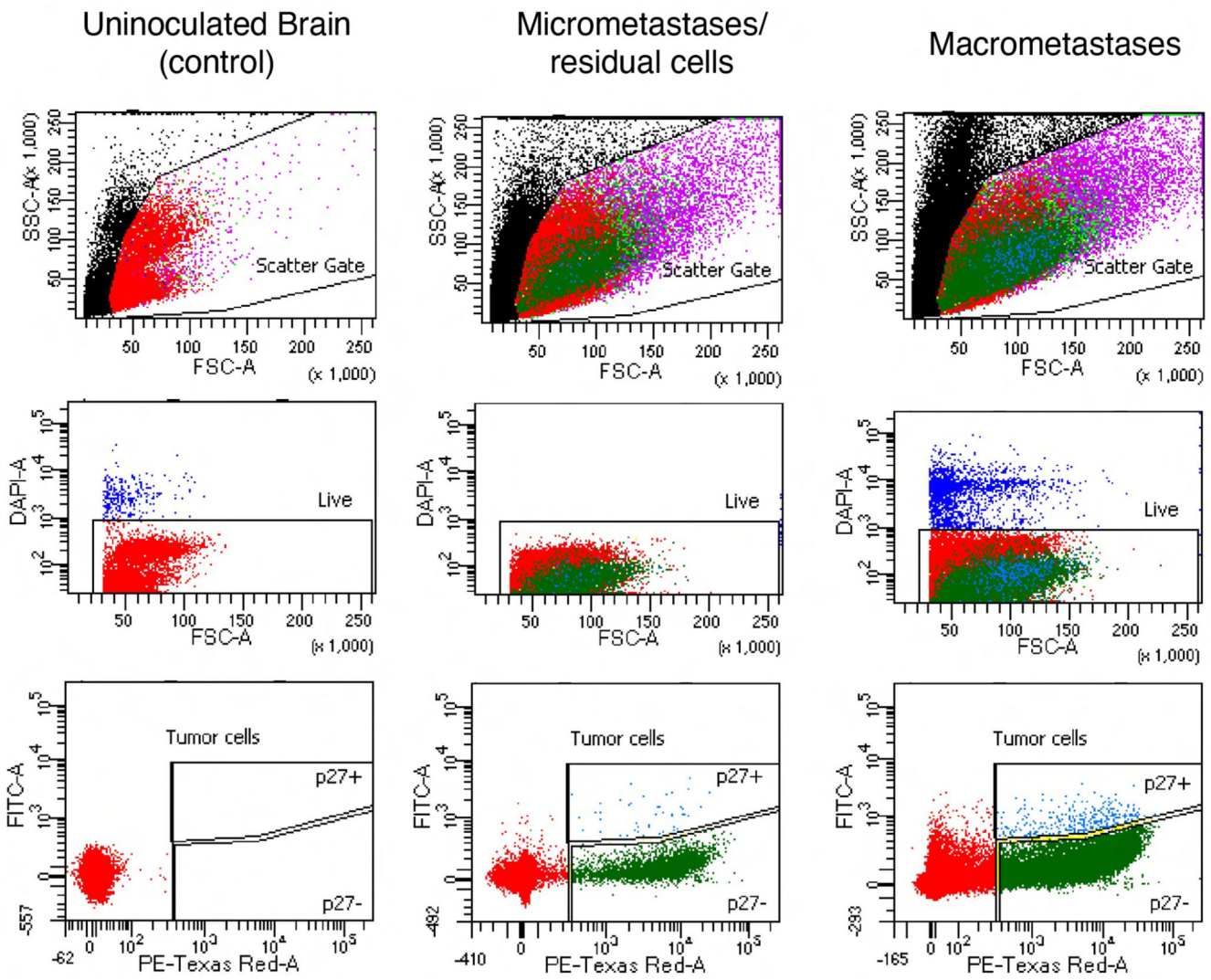

Extended Data Fig. 7: Gating strategy to flow sort tdTomato-positive brain metastases and DTCs for single cell transcriptomic analysis.

Gating strategy for isolating tdTomato+/ mVenus-p27+ micrometastases and tdTomato+/ mVenus-p27- macrometastases from brains of NOD-SCID mice inoculated with tdTomato-mVenus-p27K- T4-2 cells via ultrasound-guided intracardiac injection. Dead cells were excluded based on DAPI incorporation. Live cells were further gated off PE-Texas Red

(for tdTomato) and FITC-A (for mVenus-p27). Non-inoculated brain cell suspension and tdTomato- or mVenus-p27-expressing T4-2s were used to set gates.

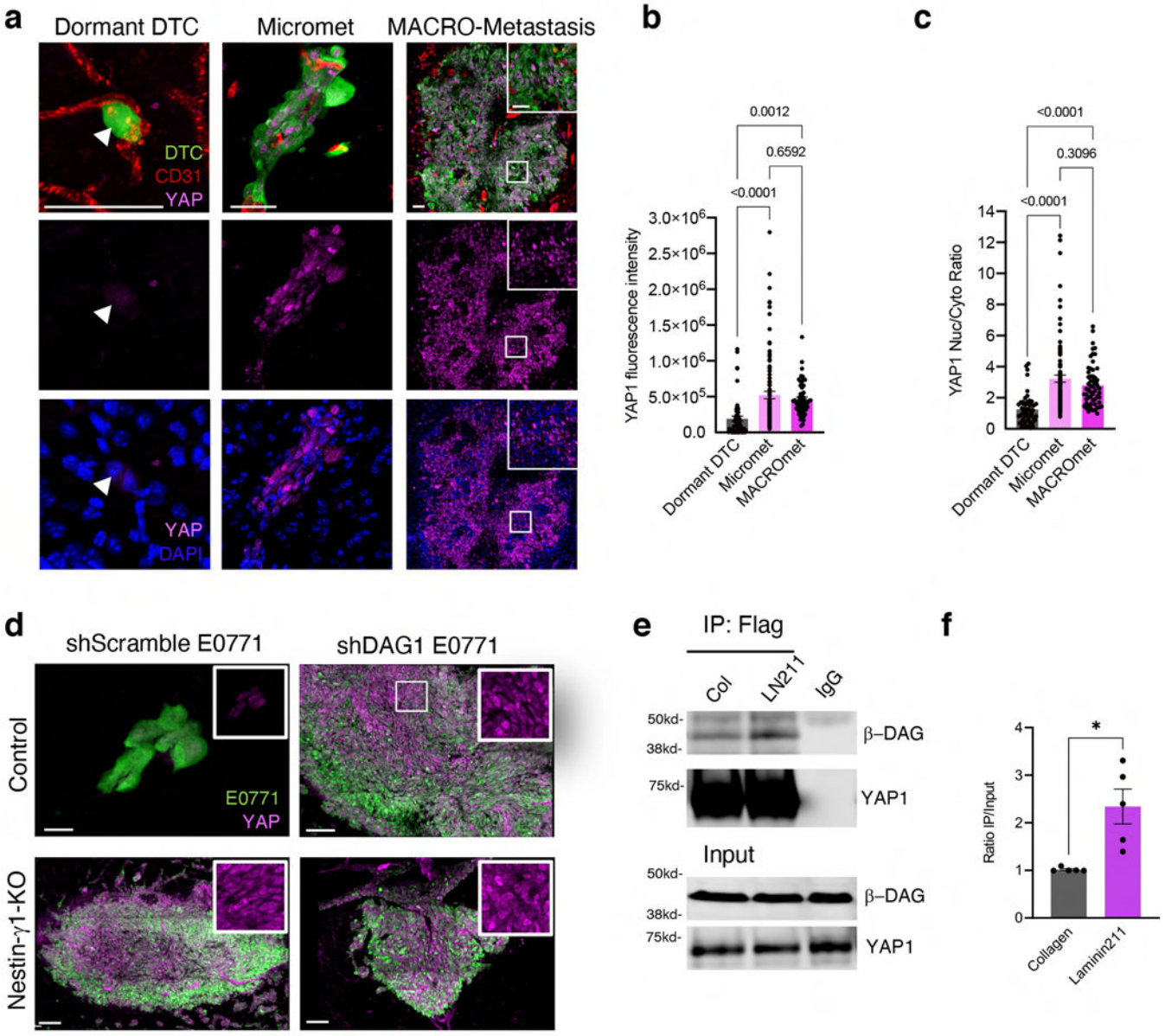

Extended Data Fig. 8: YAP localizes to the nucleus upon DTC activation in multiple models.

a) Representative IF staining for YAP1 to assess its localization and intensity in eGFP-T4-2 DTCs at different stages of metastatic progression in the brains of NOD SCID mice, ~8 weeks after intracardiac injection of eGFP-T4-2 cells. White arrowhead denotes the YAP-low nucleus of a solitary DTC. Scale bar = 50 μm. From left to right, images are representative of n = 44, 90 and 47 independent lesions imaged across n=4 mice. **b**, **c**) YAP1 fluorescent intensity (**b**) and subcellular location (**c**) were quantified for n=211 total lesions across 4 mice. P-values were calculated by one-way ANOVA and Tukey's post hoc test. **d**) Representative IF staining for YAP1 in metastatic lesions of N-γ1-KOs and control mice

inoculated with either shScramble E0771 or shDAG1 E0771. Scale bar = 10 μm for top left panel and 100 μm for other panels. Images are representative of n=3 sections imaged per mouse across n=3 mice per condition. **e**) Co-immunoprecipitation (IP) of β-DAG and YAP1. FLAG-YAP1-transduced MDA-MB-231 cells were grown on type I Collagen (Col-1) or laminin-211 (LN-211)-coated plates. ~1 mg of protein lysate was precipitated with 40 ul of FLAG-tag monoclonal antibody or control rat IgG agarose. Precipitated proteins were blotted with YAP1 and β-DAG antibodies. ~10% of the protein lysate was used as a loading control for the input. **f**) Ratio of bound β-DAG that co-immunoprecipitated with YAP1 to total β-DAG in 10% of the cell lysate for MDA-MB-231 cells grown on LN-211, normalized to the same ratio from MDA-MB-231 cells grown on Col-I to correct for the variations between independent replicates. Blots are representative of n=5 biologically independent samples probed. *P = 0.02 calculated by paired, two-tailed t-test. Data are presented as mean values +/− SEM.

Supplementary Material

Refer to Web version on PubMed Central for supplementary material.

Acknowledgements.

We are grateful to Slobodan Beronja (Fred Hutchinson Cancer Research Center, FHCRC) for reading the manuscript and providing critical feedback, and to the entire Ghajar laboratory for helpful discussions. We thank Dr. Patricia Steeg (National Cancer Institute) for generously providing us with the MDA-MB-231-BR7 cell line, Dr. Patrick Paddison (FHCRC) for ECM overexpression constructs, Dr. Valera Vasioukhin (FHCRC) for YAP mutant overexpression constructs, Dr. William Stallcup (Sanford Burnham) for generously providing us with the PDGFRβ antibody, Dr. Markus Ruegg (University of Basel) for providing agrin cDNA and antibody, Dr. Julio Vazquez Lopez and Emma Schweitzer (FHCRC) for assistance with two-photon microscopy, Dr. Frank Szulzewsky (FHCRC) for providing Cx3cr1-GFP;CCR2-RFP reporter mice, and Dr. Sidney Strickland (Rockefeller University) for contributing Lamγ1 floxed mice through The Jackson Laboratory. This study was catalyzed by start-up funds provided by the FHCRC, and supported to its completion by funding from the NIH/NCI (R01 CA252874; CMG), a Physical Sciences Oncology Project Grant from the NIH/NCI (U54CA193461-01; ECH), awards from the Department of Defense (DoD) Breast Cancer Research Program (BCRP; W841XWH-15-1-0201 to CMG and KCH; W81XWH-19-1-0076 to CMG), and by the Comparative Medicine, Experimental Histopathology and Genomics Shared Resources of the Fred Hutch/University of Washington Cancer Consortium (P30 CA015704). Rapid autopsy specimen collection at Huntsman Cancer Institute was supported by Huntsman Cancer Foundation and Halt Cancer at X. JD was supported by a Postdoctoral Breakthrough award (W81XWH-18-1-0028) by the DoD BCRP. ARL was supported by a fellowship from the NCI (F99CA234840-02). CAG was supported by a postdoctoral fellowship from the Susan G. Komen Foundation. LP was supported by Postdoc.Mobility fellowships (165389 and 177917) from the Swiss National Science Foundation. FW received funding from the Deutsche Krebshilfe (German Cancer Aid), Priority Program “Translational Oncology”, #70112507, “Preventive strategies against brain metastases.” Some autopsy materials used in this study were obtained from the University of Washington Neuropathology Core, which is supported by the Alzheimer’s Disease Research Center (AG05136), the Adult Changes in Thought Study (AG006781), and Morris K. Udall Center of Excellence for Parkinson’s Disease Research (NS062684). The funders had no role in study design, data collection and analysis, decision to publish or preparation of the manuscript.

References.

1. Steeg PS, Camphausen KA & Smith QR. Brain metastases as preventive and therapeutic targets. Nature reviews. Cancer 11, 352–363 (2011). [PubMed: 21472002]
2. Quail DF. & Joyce JA. The Microenvironmental Landscape of Brain Tumors. Cancer cell 31, 326–341 (2017). [PubMed: 28292436]
3. Zimmer AS. et al. Temozolomide in secondary prevention of HER2-positive breast cancer brain metastases. Future Oncol 16, 899–909 (2020). [PubMed: 32270710]

4. Lorger M. & Felding-Habermann B. Capturing changes in the brain microenvironment during initial steps of breast cancer brain metastasis. The American journal of pathology 176, 2958–2971 (2010). [PubMed: 20382702]
5. Bos PD. et al. Genes that mediate breast cancer metastasis to the brain. Nature 459, 1005–1009 (2009). [PubMed: 19421193]
6. Joyce JA. & Pollard JW. Microenvironmental regulation of metastasis. Nature reviews. *Cancer* 9, 239–252 (2009). [PubMed: 19279573]
7. Witzel I, Oliveira-Ferrer L, Pantel K, Muller V. & Wikman H. Breast cancer brain metastases: biology and new clinical perspectives. *Breast cancer research :* BCR 18, 8 (2016). [PubMed: 26781299]
8. Paget S. The distribution of secondary growths in cancer of the breast. 1889. Cancer metastasis reviews 8, 98–101 (1989). [PubMed: 2673568]
9. Noltenius C. & Noltenius H. Dormant tumor cells in liver and brain. An autopsy study on metastasizing tumors. Pathology, research and practice 179, 504–511 (1985). [PubMed: 4001027]
10. Heyn C. et al. In vivo MRI of cancer cell fate at the single-cell level in a mouse model of breast cancer metastasis to the brain. Magn Reson Med 56, 1001–1010 (2006). [PubMed: 17029229]
11. Ghajar CM. et al. The perivascular niche regulates breast tumour dormancy. Nature cell biology 15, 807–817 (2013). [PubMed: 23728425]
12. Carlson P. et al. Targeting the perivascular niche sensitizes disseminated tumour cells to chemotherapy. Nature cell biology 21, 238–250 (2019). [PubMed: 30664790]
13. Price TT. et al. Dormant breast cancer micrometastases reside in specific bone marrow niches that regulate their transit to and from bone. Science translational medicine 8, 340ra373 (2016).
14. Kienast Y. et al. Real-time imaging reveals the single steps of brain metastasis formation. Nature medicine 16, 116–122 (2010).
15. Stoletov K. et al. Role of connexins in metastatic breast cancer and melanoma brain colonization. Journal of cell science 126, 904–913 (2013). [PubMed: 23321642]
16. Carbonell WS, Ansorge O, Sibson N. & Muschel R. The vascular basement membrane as “soil” in brain metastasis. PloS one 4, e5857 (2009). [PubMed: 19516901]
17. Er EE. et al. Pericyte-like spreading by disseminated cancer cells activates YAP and MRTF for metastatic colonization. Nature cell biology 20, 966–978 (2018). [PubMed: 30038252]
18. Janzer RC. & Raff MC. Astrocytes induce blood-brain barrier properties in endothelial cells. Nature 325, 253–257 (1987). [PubMed: 3543687]
19. Armulik A. et al. Pericytes regulate the blood-brain barrier. Nature 468, 557–561 (2010). [PubMed: 20944627]
20. Liddelow S. & Barres B. SnapShot: Astrocytes in Health and Disease. Cell 162, 1170-1170 e1171 (2015). [PubMed: 26317476]
21. Ridet JL, Malhotra SK, Privat A. & Gage FH. Reactive astrocytes: cellular and molecular cues to biological function. Trends Neurosci 20, 570–577 (1997). [PubMed: 9416670]
22. Contreras-Zarate MJ. et al. Estradiol induces BDNF/TrkB signaling in triple-negative breast cancer to promote brain metastases. Oncogene 38, 4685–4699 (2019). [PubMed: 30796353]
23. Marchetti D, Li J. & Shen R. Astrocytes contribute to the brain-metastatic specificity of melanoma cells by producing heparanase. Cancer research 60, 4767–4770 (2000). [PubMed: 10987284]
24. Doron H. et al. Inflammatory Activation of Astrocytes Facilitates Melanoma Brain Tropism via the CXCL10-CXCR3 Signaling Axis. Cell reports 28, 1785–1798 e1786 (2019). [PubMed: 31412247]
25. Zhang L. et al. Microenvironment-induced PTEN loss by exosomal microRNA primes brain metastasis outgrowth. Nature 527, 100–104 (2015). [PubMed: 26479035]
26. Palmieri D. et al. Her-2 overexpression increases the metastatic outgrowth of breast cancer cells in the brain. Cancer research 67, 4190–4198 (2007). [PubMed: 17483330]
27. Abbott NJ, Ronnback L. & Hansson E. Astrocyte-endothelial interactions at the blood-brain barrier. Nature reviews. Neuroscience 7, 41–53 (2006). [PubMed: 16371949]
28. Nagelhus EA. & Ottersen OP. Physiological roles of aquaporin-4 in brain. Physiol Rev 93, 1543–1562 (2013). [PubMed: 24137016]

29. Sixt M. et al. Endothelial cell laminin isoforms, laminins 8 and 10, play decisive roles in T cell recruitment across the blood-brain barrier in experimental autoimmune encephalomyelitis. The Journal of cell biology 153, 933–946 (2001). [PubMed: 11381080]
30. Agrawal S. et al. Dystroglycan is selectively cleaved at the parenchymal basement membrane at sites of leukocyte extravasation in experimental autoimmune encephalomyelitis. The Journal of experimental medicine 203, 1007–1019 (2006). [PubMed: 16585265]
31. Menezes MJ. et al. The extracellular matrix protein laminin alpha2 regulates the maturation and function of the blood-brain barrier. J Neurosci 34, 15260–15280 (2014). [PubMed: 25392494]
32. Berzin TM. et al. Agrin and microvascular damage in Alzheimer's disease. Neurobiol Aging 21, 349–355 (2000). [PubMed: 10867220]
33. Willis RA. The spread of tumours in the human body. (Butterworth & Co. (Publishers), Ltd., London, England; 1952).
34. Wasilewski D, Priego N, Fustero-Torre C. & Valiente M. Reactive Astrocytes in Brain Metastasis. Front Oncol 7, 298 (2017). [PubMed: 29312881]
35. Seandel M. et al. Generation of a functional and durable vascular niche by the adenoviral E4ORF1 gene. Proceedings of the National Academy of Sciences of the United States of America 105, 19288–19293 (2008). [PubMed: 19036927]
36. Vanlandewijck M. et al. A molecular atlas of cell types and zonation in the brain vasculature. Nature 554, 475–480 (2018). [PubMed: 29443965]
37. Liu J. et al. A human cell type similar to murine central nervous system perivascular fibroblasts. Experimental cell research 402, 112576 (2021). [PubMed: 33798592]
38. Zhang Y. et al. An RNA-sequencing transcriptome and splicing database of glia, neurons, and vascular cells of the cerebral cortex. J Neurosci 34, 11929–11947 (2014). [PubMed: 25186741]
39. Yurchenco PD. Basement membranes: cell scaffoldings and signaling platforms. Cold Spring Harbor perspectives in biology 3 (2011).
40. Cimino PJ Jr. & Perrin RJ. Mammaglobin-A immunohistochemistry in primary central nervous system neoplasms and intracranial metastatic breast carcinoma. Appl Immunohistochem Mol Morphol 22, 442–448 (2014). [PubMed: 23958549]
41. Yao Y, Chen ZL, Norris EH. & Strickland S. Astrocytic laminin regulates pericyte differentiation and maintains blood brain barrier integrity. Nature communications 5, 3413 (2014).
42. Chen ZL. et al. Ablation of astrocytic laminin impairs vascular smooth muscle cell function and leads to hemorrhagic stroke. The Journal of cell biology 202, 381–395 (2013). [PubMed: 23857767]
43. Cheng YS, Champliaud MF, Burgeson RE, Marinkovich MP. & Yurchenco PD. Self-assembly of laminin isoforms. The Journal of biological chemistry 272, 31525–31532 (1997). [PubMed: 9395489]
44. Malhotra D. et al. Tolerance is established in polyclonal CD4(+) T cells by distinct mechanisms, according to self-peptide expression patterns. Nat Immunol 17, 187–195 (2016). [PubMed: 26726812]
45. Campbell KP. & Kahl SD. Association of dystrophin and an integral membrane glycoprotein. Nature 338, 259–262 (1989). [PubMed: 2493582]
46. Weaver VM. et al. Reversion of the malignant phenotype of human breast cells in three-dimensional culture and in vivo by integrin blocking antibodies. The Journal of cell biology 137, 231–245 (1997). [PubMed: 9105051]
47. Gumbiner BM. & Kim NG. The Hippo-YAP signaling pathway and contact inhibition of growth. Journal of cell science 127, 709–717 (2014). [PubMed: 24532814]
48. Wang Y. et al. Comprehensive Molecular Characterization of the Hippo Signaling Pathway in Cancer. Cell reports 25, 1304–1317 e1305 (2018). [PubMed: 30380420]
49. Cheung TH. & Rando TA. Molecular regulation of stem cell quiescence. Nat Rev Mol Cell Biol 14, 329–340 (2013). [PubMed: 23698583]
50. Lin Z. et al. Decoding WW domain tandem-mediated target recognitions in tissue growth and cell polarity. Elife 8 (2019).

51. Morikawa Y, Heallen T, Leach J, Xiao Y. & Martin JF. Dystrophin-glycoprotein complex sequesters Yap to inhibit cardiomyocyte proliferation. Nature 547, 227–231 (2017). [PubMed: 28581498]
52. Fredriksson S. et al. Protein detection using proximity-dependent DNA ligation assays. Nature biotechnology 20, 473–477 (2002).
53. Zhao B. et al. Inactivation of YAP oncoprotein by the Hippo pathway is involved in cell contact inhibition and tissue growth control. Genes & development 21, 2747–2761 (2007). [PubMed: 17974916]
54. Zhao B, Li L, Tumaneng K, Wang CY. & Guan KL. A coordinated phosphorylation by Lats and CK1 regulates YAP stability through SCF(beta-TRCP). Genes & development 24, 72–85 (2010). [PubMed: 20048001]
55. Zhao B. et al. TEAD mediates YAP-dependent gene induction and growth control. Genes & development 22, 1962–1971 (2008). [PubMed: 18579750]
56. Albrengues J. et al. Neutrophil extracellular traps produced during inflammation awaken dormant cancer cells in mice. Science 361 (2018).
57. Ghajar CM. Metastasis prevention by targeting the dormant niche. Nature reviews. Cancer 15, 238–247 (2015). [PubMed: 25801619]
58. Martin PT. Mechanisms of disease: congenital muscular dystrophies-glycosylation takes center stage. Nat Clin Pract Neurol 2, 222–230 (2006). [PubMed: 16932553]

Methods only:

59. Tronche F. et al. Disruption of the glucocorticoid receptor gene in the nervous system results in reduced anxiety. Nat Genet 23, 99–103 (1999). [PubMed: 10471508]
60. Chen ZL. & Strickland S. Laminin gamma1 is critical for Schwann cell differentiation, axon myelination, and regeneration in the peripheral nerve. J Cell Biol 163, 889–899 (2003). [PubMed: 14638863]
61. Saederup N. et al. Selective chemokine receptor usage by central nervous system myeloid cells in CCR2-red fluorescent protein knock-in mice. PloS one 5, e13693 (2010).
62. Briand P, Nielsen KV, Madsen MW. & Petersen OW. Trisomy 7p and malignant transformation of human breast epithelial cells following epidermal growth factor withdrawal. Cancer research 56, 2039–2044 (1996). [PubMed: 8616848]
63. Cailleau R, Olive M. & Cruciger QV. Long-term human breast carcinoma cell lines of metastatic origin: preliminary characterization. In Vitro 14, 911–915 (1978). [PubMed: 730202]
64. Yoneda T, Williams PJ, Hiraga T, Niewolna M. & Nishimura R. A bone-seeking clone exhibits different biological properties from the MDA-MB-231 parental human breast cancer cells and a brain-seeking clone in vivo and in vitro. Journal of bone and mineral research : the official journal of the American Society for Bone and Mineral Research 16, 1486–1495 (2001).
65. Harper KL. et al. Mechanism of early dissemination and metastasis in Her2(+) mammary cancer. Nature 540, 588–592 (2016). [PubMed: 27974798]
66. She W. et al. Chromatin reprogramming during the somatic-to-reproductive cell fate transition in plants. Development 140, 4008–4019 (2013). [PubMed: 24004947]
67. Zheng GX. et al. Massively parallel digital transcriptional profiling of single cells. Nature communications 8, 14049 (2017).
68. Wolf FA, Angerer P. & Theis FJ. SCANPY: large-scale single-cell gene expression data analysis. Genome Biol 19, 15 (2018). [PubMed: 29409532]
69. Tarashansky AJ, Xue Y, Li P, Quake SR. & Wang B. Self-assembling manifolds in single-cell RNA sequencing data. Elife 8 (2019).
70. Satija R, Farrell JA, Gennert D, Schier AF. & Regev A. Spatial reconstruction of single-cell gene expression data. Nat Biotechnol 33, 495–502 (2015). [PubMed: 25867923]
71. Yang X. et al. A public genome-scale lentiviral expression library of human ORFs. Nature methods 8, 659–661 (2011). [PubMed: 21706014]

72. Oki T. et al. A novel cell-cycle-indicator, mVenus-p27K-, identifies quiescent cells and visualizes G0-G1 transition. Scientific reports 4, 4012 (2014). [PubMed: 24500246]

73. Li P. et al. alphaE-catenin inhibits a Src-YAP1 oncogenic module that couples tyrosine kinases and the effector of Hippo signaling pathway. Genes & development 30, 798–811 (2016). [PubMed: 27013234]

74. Ganesh K. et al. L1CAM defines the regenerative origin of metastasis-initiating cells in colorectal cancer. Nat Cancer 1, 28–45 (2020). [PubMed: 32656539]

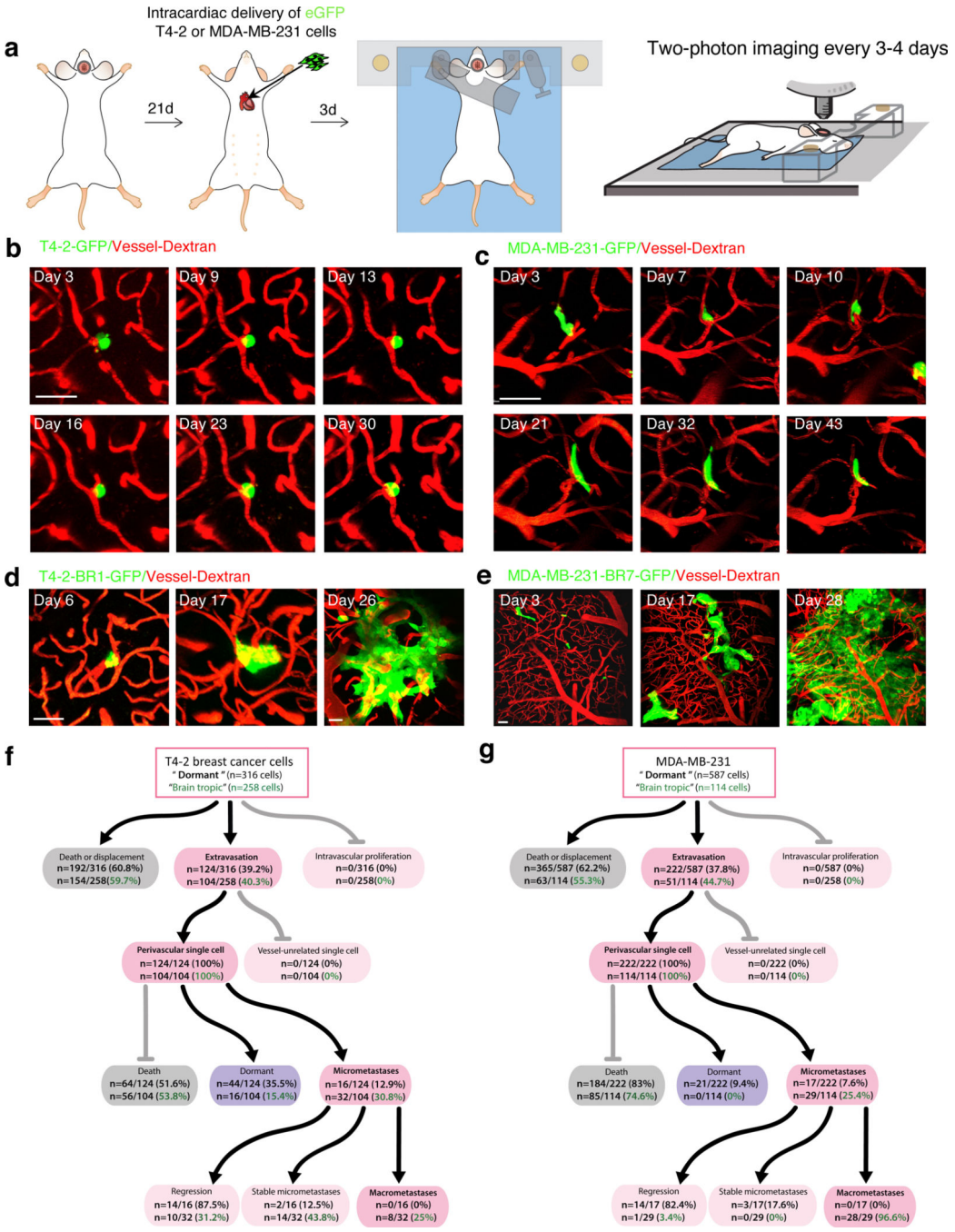

Figure 1. Intravital imaging reveals that escape from dormancy is the rate limiting step for breast cancer brain metastasis.

a) Experimental schematic: An open-skull cranial window was implanted in 6–8 week old NOD-SCID female mice. After 3 weeks, 1×10^6 eGFP-T4-2 or -T4-2-BR1; or 5×10^5 eGFP-MDA-MB-231 or -MDA-MB-231-BR7 TNBC cells were delivered by ultrasound-guided intracardiac injection. Three days later, mice were anesthetized and mounted onto a custom stage for two-photon imaging. Mice were subsequently imaged every 3–4 days for up to two-months. **b, c**) Image series acquired from the brains of mice inoculated with parental

(**b**) eGFP-T4-2 cells (n = 316 cells over 6 mice) or (**c**) eGFP-MDA-MB-231 cells (n = 587 cells over 6 mice), or brain-tropic (**d**) eGFP-T4-2-BR1 cells (n = 258 cells over 5 mice) or (**e**) eGFP-MDA-MB-231-BR7 cells (n = 114 cells over 5 mice). Tumour inoculated mice were perfused with TRITC dextran (MW=500 kDa) to mark vasculature. Scale bar = 40 μm. **f, g**) A quantitative description of the fate of distinct (**f**) latent T4-2 cells or brain-tropic T4-2-BR1 cells and (**g**) latent MDA-MB-231 cells or brain-tropic MDA-MB-231-BR7 cells over the course of 4 to 7 weeks post-injection, establishing rates of extravasation, cell death, persistent single cells, micrometastatic progression and transition to metastases for each cell line. The number of cells detected in static images at different steps of metastasis is indicated in the diagram, and percentages represent the fraction of cells from the previous step of the metastatic cascade.

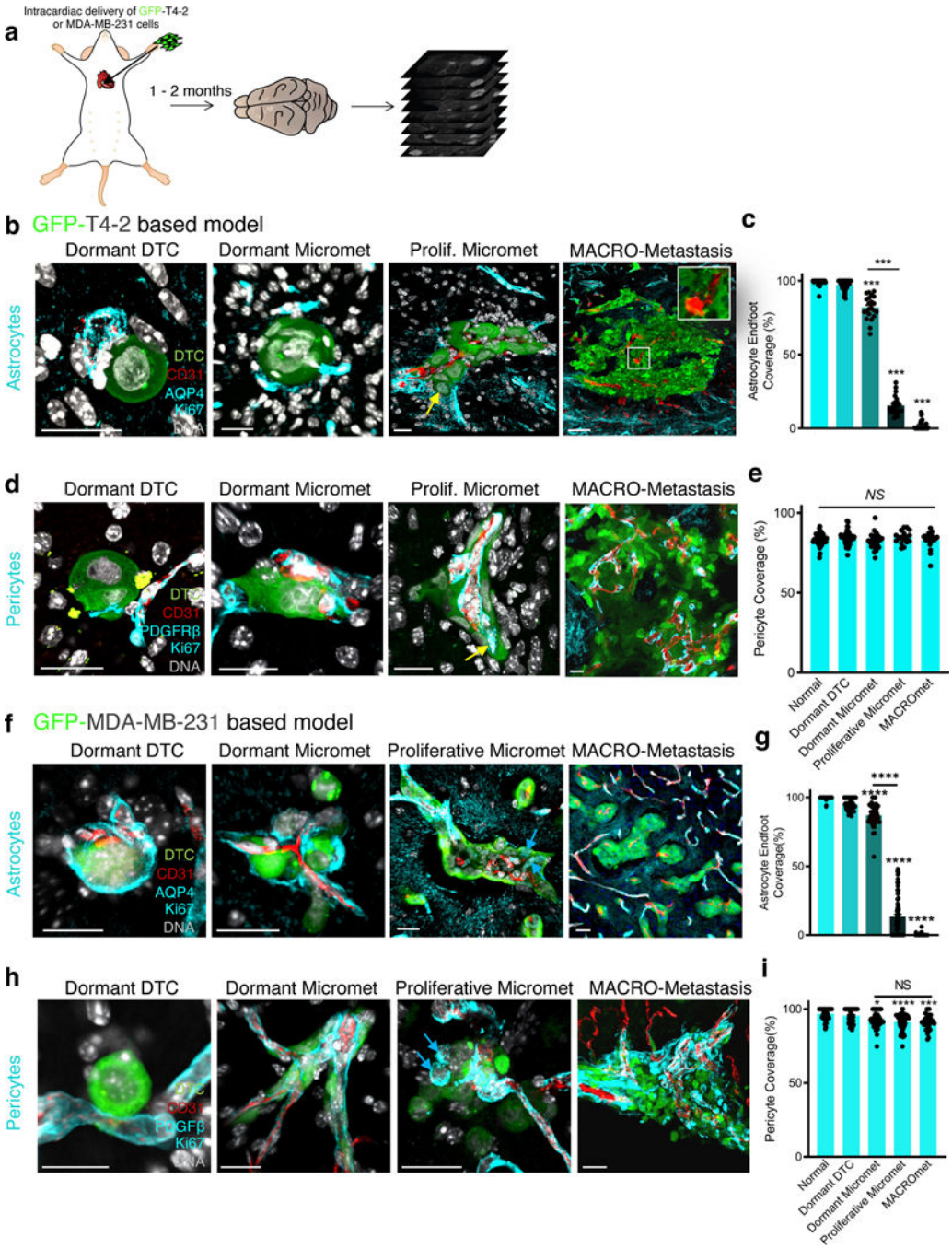

Figure 2. Astrocyte endfeet are stripped from DTC-associated vessels upon activation of micrometastases.

a) Schematic of an experiment designed to investigate the association of perivascular cells with DTCs over the course of metastatic progression in the brain. 1×10^5 eGFP-T4-2 or mCherry-MDA-MB-231 breast cancer cells were injected into 6–8 week old NOD-SCID female mice by ultrasound guided intracardiac injection. Serial coronal sections covering the entire mouse brain (~250 sections/brain) were stained and analyzed 6–8 weeks later. **b, f**) Representative IF staining of $AQP4^+$ astrocyte endfoot coverage of DTC-associated

microvessels across four stages of brain metastatic progression for (**b**) T4-2 and (**f**) MDA-MB-231 models. Arrows indicate Ki67$^+$ cells. Scale bar = 20 μm. From left to right, images are representative of n = 60, 22, 25 and 28 independent lesions imaged across n=5 mice in panel (**b**), and of n = 54, 43, 74 and 38 independent lesions across n=4 mice in panel (**f**). **c, g**) Astrocyte endfoot coverage of DTC-associated vessels in (**c**) T4-2 and (**g**) MDA-MB-231 models, quantified for n=169 (T4-2) across 5 mice and n=286 (MDA-MB-231) total lesions across 4 mice. ***P<0.001 (T4-2) and ****P<0.00001 (MDA-MB-231) by one-way ANOVA, followed by Tukey's post hoc test. **d, h**) Representative IF staining of PDGFRß$^+$ pericyte coverage of DTC-associated microvessels for (**d**) T4-2 and (**h**) MDA-MB-231 models. Arrows indicate Ki67$^+$ cells in proliferative micrometastases. Scale bar = 20 μm. From left to right, images are representative of n = 60, 24, 17 and 23 independent lesions imaged across n=5 mice in panel (**d**), and n = 56, 54, 51 and 34 independent lesions across n=4 mice in panel (**h**). **e, i**) Pericyte coverage of DTC-associated vessels, quantified for n=171 T4-2 lesions across n=5 mice and n=280 MDA-MB-231 lesions across n=4 mice. *NS* denotes no significance for all comparisons of T4-2-associated vessels (all P-values > 0.33) by one-way ANOVA, followed by Tukey's post hoc test in panel (**e**). *NS* denotes no significance (P>0.28) across indicated conditions in panel (**i**), whereas ****P<0.0001, ***P=0.0004, *P=0.036 versus dormant DTCs by one-way ANOVA and Dunnett's multiple comparisons test. All data are presented as mean values +/− SEM.

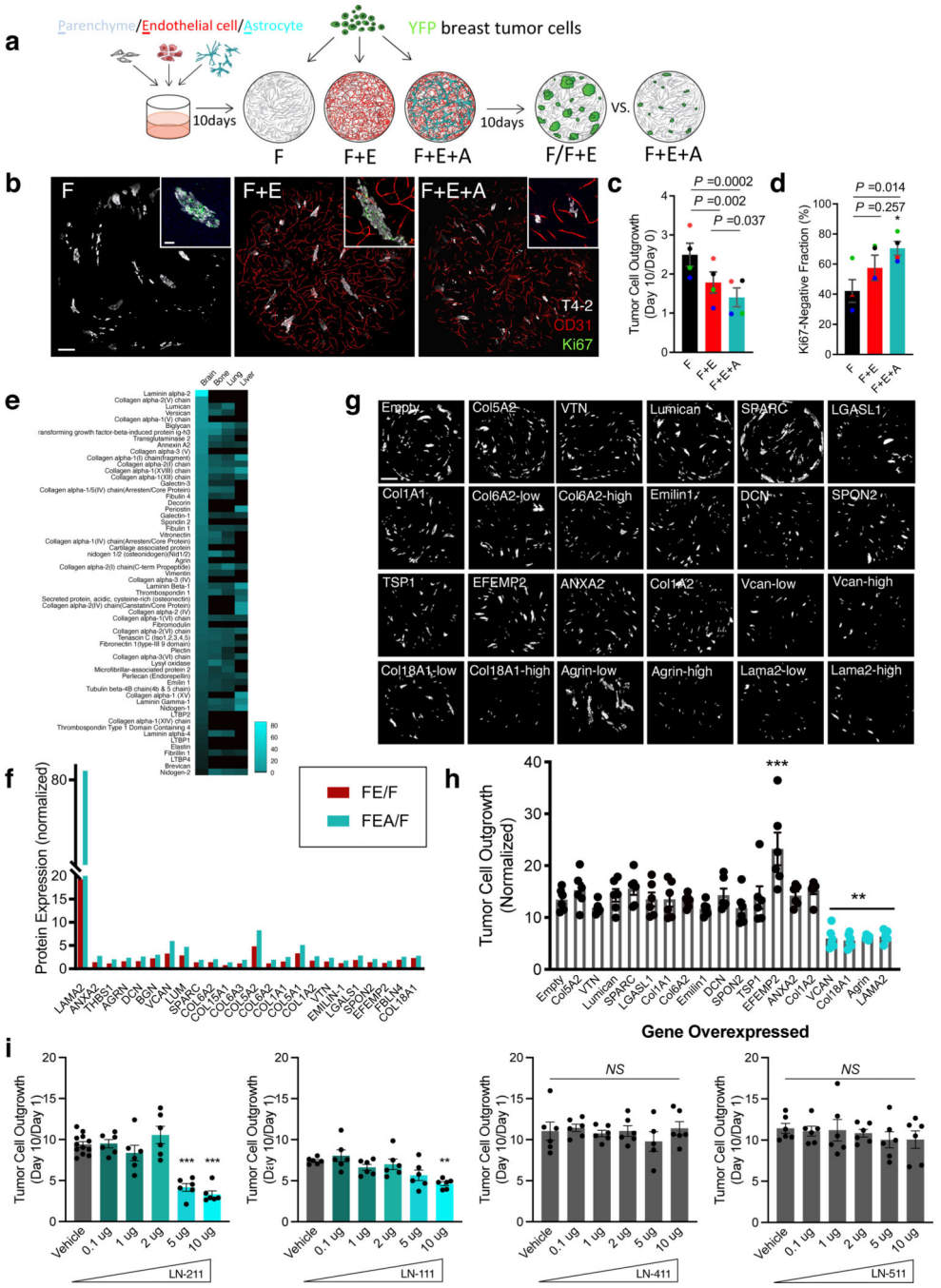

Figure 3. A culture-based mimetic of the brain's perivascular niche suggests astrocytic laminin-α2 suppresses DTC outgrowth.

a) Combinations of primary human brain adventitial fibroblasts (F), endothelial cells (E), and astrocytes (A) self-assembled into brain vascular-like structures over 10 days. YFP-expressing T4-2 cells were then seeded sparsely (100 cells/well) in serum-free media onto these cultures. Entire wells were imaged immediately after seeding BCCs and again 10 days later to quantify tumour cell outgrowth. **b**) Representative IF images of T4-2 cell outgrowth in F vs. F+E vs. F+E+A 10 days post-seeding. Scale bar = 500 μm. Insets illustrate Ki67

status of T4-2 cells/clusters on F, F+E and F+E+A clusters. Scale bar = 100 μm. Images are representative of n=6 sets of co-cultures tile-scanned per condition across n=4 biologically independent experiments. **c**) Tumour cell area fraction of YFP-T4-2 at day 10, normalized to area fraction at initial seeding, and **d**) percentage of Ki67-negative tumour cell clusters at day 10 (n = 6 sets of co-cultures analyzed per condition, 4 independent experiments each indicated by a different color). *P*-values were calculated using one-way ANOVA followed by Tukey's post hoc test. **e**) Heatmap of ECM protein spectral counts from brain-, bone marrow-, lung- and liver-like perivascular niche cultures, shown in descending order after normalizing to their respective stroma. Intensity scale at lower right. Samples from n=3 biologically independent experiments were pooled. **f**) Fold change of the top 24 ECM factors identified in (**e**) for F+E+A and F+E, normalized to F (n = 6 independent sets of co-cultures were pooled analyzed per condition). **g**) Representative 96-well tile scans of T4-2 outgrowth on HBAF expressing the indicated lentiviral overexpression construct, 10 days post-seeding. **h**) Quantification of T4-2 outgrowth at this timepoint (n = 6 independent sets analyzed per condition). ***P=0.0005 (ANXA2), **P=0.0011 (VCAN), 0.0005 (Col18A1), 0.0017 (Agrin) and 0.0022 (LAMA2) versus empty vector, by one-way ANOVA and Dunnett's multiple comparisons test. **i**) T4-2 outgrowth on HBAF, following laminin (LN)-211, −111, −411 or −511 spike-in (n=6 sets of co-cultures analyzed per condition across 3 independent experiments). **P=0.0025, ***P<0.0001 versus vehicle by one-way ANOVA and Dunnett's multiple comparisons test. *NS* indicates no significance (P-values > 0.69). All data are presented as mean values +/− SEM.

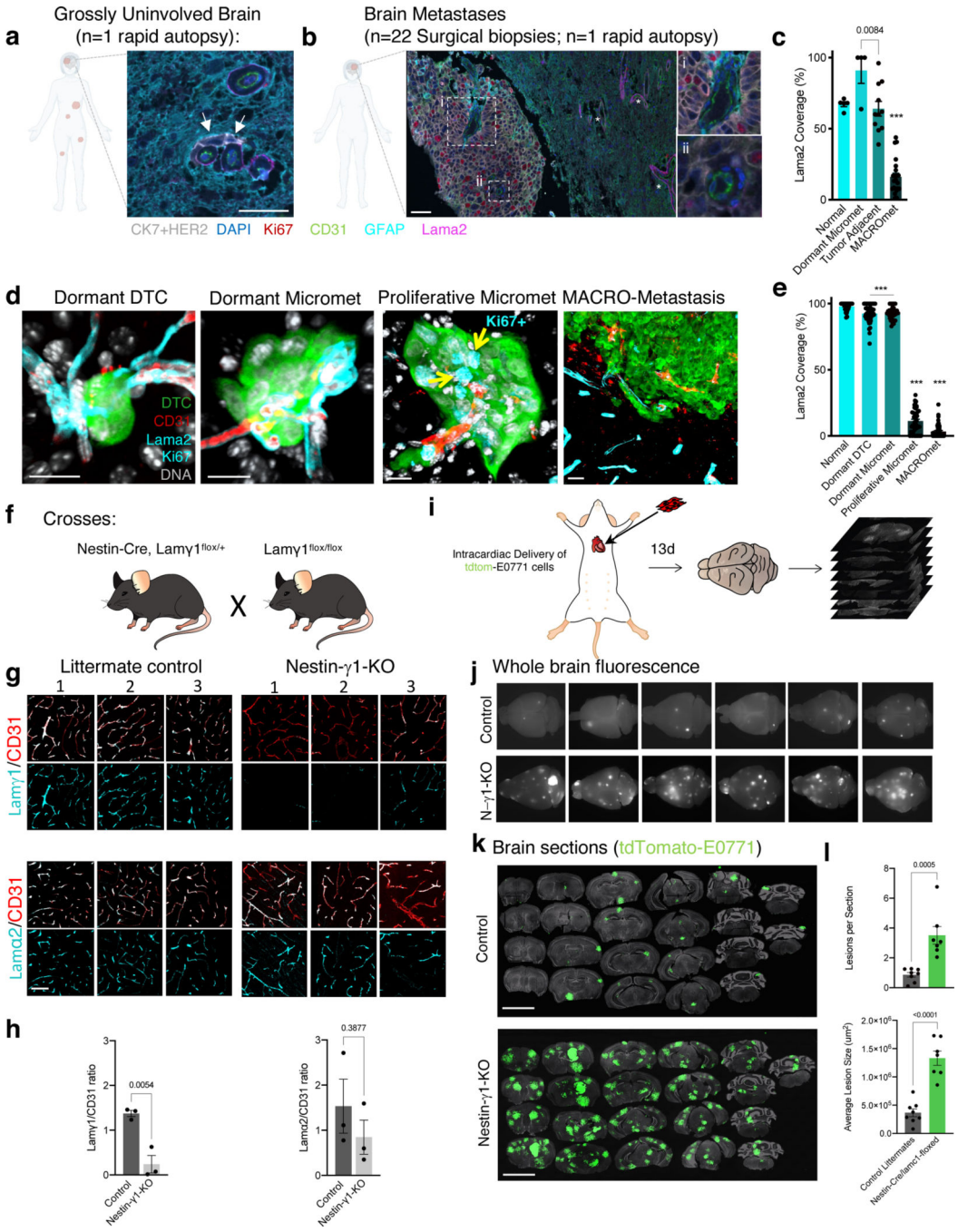

Figure 4: Loss of astrocytic laminins coincides with DTC proliferation in humans and in mice.

a) Representative multiplex IHC staining for laminin-α2 (laminin-α2, magenta) and GFAP (cyan) to assess astrocyte vessel coverage in Ki67^{-} micrometastases detected in grossly uninvolved regions of breast cancer patient brain tissue. White arrows indicate a CK7/Her2^{+} cluster of two Ki67^{-} DTCs. Scale bar = 50 μm. Imaged representative of n=4 dormant micrometastases from the brain of one metastatic breast cancer patient. **b**) Representative tile scan covering a whole metastatic brain lesion and adjacent tissue from a surgical biopsy, stained for indicated markers via multiplex IHC. Scale bar = 50 μm. Image representative

of n=22 brain metastases imaged across n=22 metastatic breast cancer patients. **i-ii**) *Insets*, vessels embedded within the metastatic lesion display absence of perivascular Laminin-α2. **c**) Fraction of vessels with laminin-α2 coverage was quantified for four separate Ki67$^-$ dormant micrometastases in uninvolved brain tissue from one metastatic breast cancer patient, n=1 brain metastasis ("MACROmet") from the same patient, tissue from n=22 surgical resections of breast cancer brain metastasis and the fraction of these (n=11) with non-necrotic, intact parenchyma attached ("Tumor adjacent"). Normal brain tissue from five patients diagnosed with non-cancerous neurological disease was used as a control. ***P<0.0001 comparing laminin-α2 coverage of microvessels within brain metastases to all other conditions, by one-way ANOVA and Tukey's post hoc test. **d**) Representative IF staining of laminin-α2 of eGFP-T4-2 DTC-associated microvessels. Arrows indicate Ki67+ cells in proliferative micrometastases. Scale bar = 20 μm for first three panels, and 50 μm for MACRO-metastasis panel. **e**) Quantification of laminin-α2 coverage for n=222 total lesions across 4 mice. ***P<0.001 across all conditions, by one-way ANOVA and Tukey's post hoc test. **f**) Breeding strategy to generate astrocyte-specific knockout of laminin-γ1. **g**) Representative IF staining of Laminin-γ1 and Laminin-α2 in brain from Nestin-Cre, Lamγ1$^{flox/flox}$ conditional knockout (N-γ1-KO) mice and littermate controls. Scale bar = 30 μm. Images representative of n = 6 sections analyzed per mouse; representative images for all 3 mice shown. **h**) Quantification of Laminin-γ1 and Laminin-α2 coverage normalized to vessel area in brains of N-γ1-KO mice and control littermates (data from n=6 sections per mouse averaged across 3 mice per condition). Stated *P*-values calculated via unpaired, two-tailed t-test. **i**) Experimental schematic for comparison of brain metastasis in N-γ1-KOs vs. control littermates. **j**) Ex vivo fluorescence of whole brains and **k**) representative tilescans of sectioned brains from N-γ1-KOs or their control littermates 13-days post-intracardiac injection with tdTomato-E0771. Scale bar = 5 mm. Images representative of n=20–25 sections mounted per mouse across n=8 control mice and n=7 N-γ1-KO mice. **l**) Quantification of number of lesions per brain section (*top panel*) and average lesion size (*bottom panel*). Stated *P*-value calculated via unpaired two-tailed t-test. All data are presented as mean values +/− SEM.

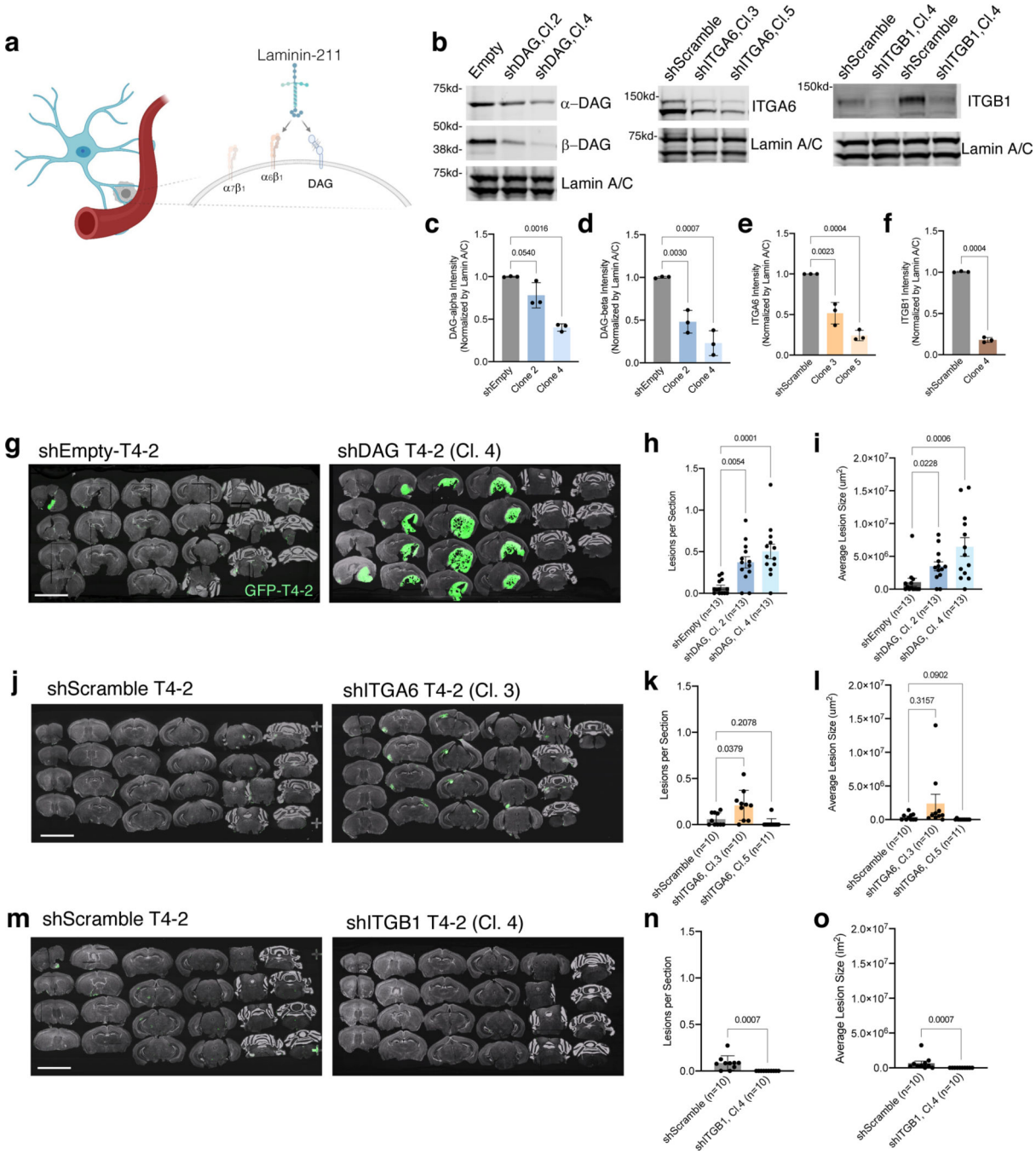

Figure 5: DTC dystroglycan is the principal transducer of astrocytic laminin-mediated quiescence.

a) Schematic illustrating potential receptors for astrocytic laminin-211 on DTCs, including dystroglycan (**DAG**) and integrin-$\alpha_6\beta_1$. Integrin-$\alpha_7\beta_1$ was not expressed by the cell lines we tested. **b**) Representative immunoblot of T4-2 clones (Cl.) infected with non-targeting shRNA (Empty or shScramble) or constructs targeting human DAG1, integrin-α_6 (ITGA6), or integrin-β_1 (ITGB1) respectively. Blots were stained for α- and β-DAG subunits (*left panel*), ITGA6 (*middle panel*), or ITGB1 (*right panel*). Lamin A/C was used as a loading

control. Blots representative of n=3 biologically independent experiments. **c-f**) Integrated intensity of α-DAG, β-DAG, ITGA6, and ITGB1 bands normalized first to their respective loading control band, then to the shEmpty or shScramble band on each blot. *P*-values were calculated by one-way ANOVA and Tukey's post hoc test (**c, d ,e**) or paired two-tailed t-test (**f**) across n=3 biologically independent experiments. **g, j, m**) Representative tilescans of brain sections from NOD-SCID mice (20–25 sections/brain) inoculated with $eGFP^+$ (**g**) shDAG1-T4-2 (n = 13 mice per group), (**j**) shITGA6-T4-2 (n = 10–11 mice per group), or (**m**) shITGB1-T4-2 (n = 10–11 mice per group), and respective shEmpty or shScramble controls, 6–8 weeks post-intracardiac injection. Scale bar = 5 mm. One to two clones were tested in each knockdown experiment. Tilescans were quantified for (**h, k, n**) number of lesions per brain section and (**i, l, o**) average lesion size, with respect to each cell line. *P*-values were calculated by one-way ANOVA and Dunnett's multiple comparisons test. All data are presented as mean values +/− SEM.

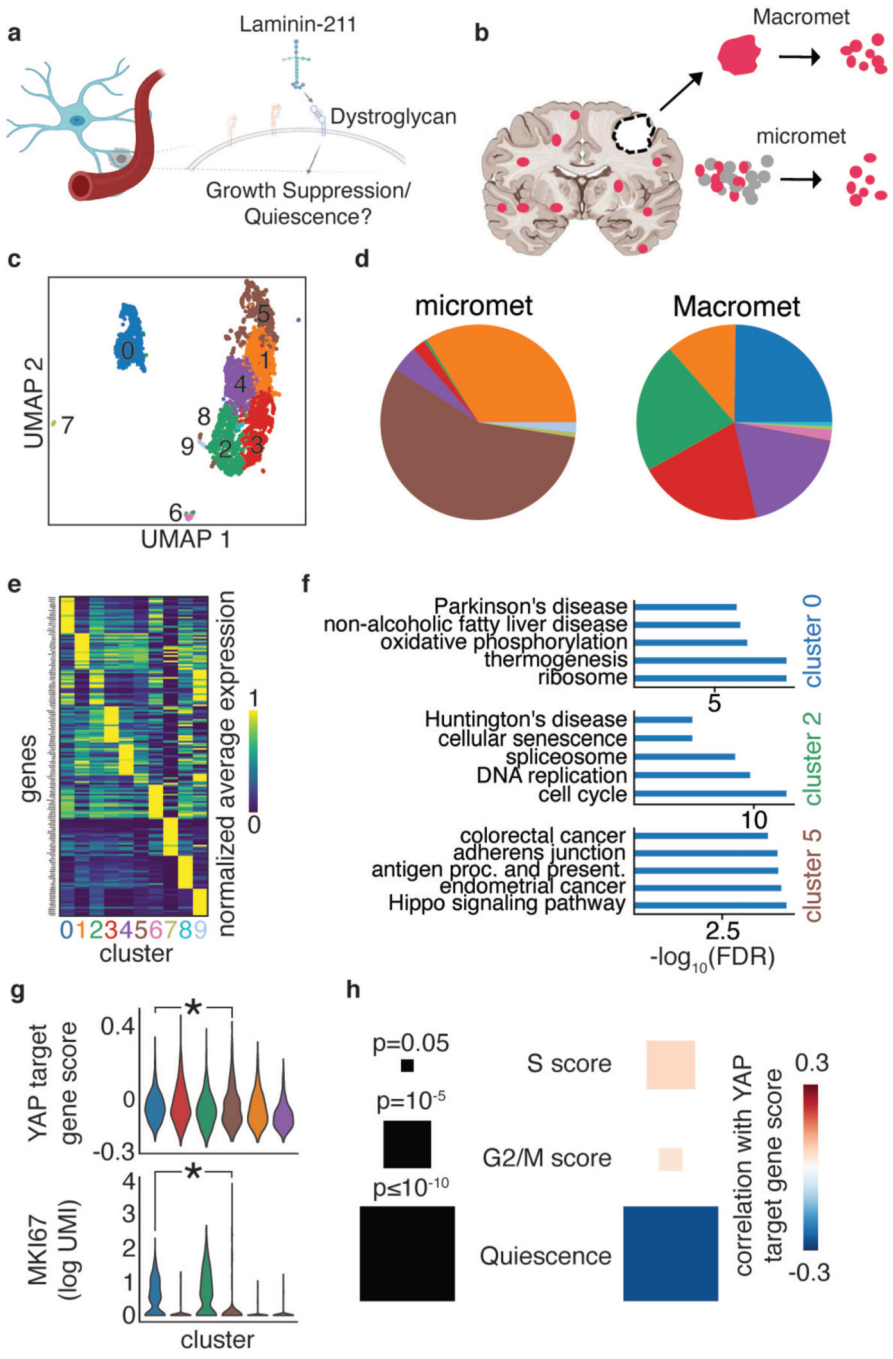

Figure 6: Single cell sequencing data suggest that YAP signaling is suppressed in DTCs.

a) A model for the laminin-211-DAG signaling axis that drives DTC quiescence. **b**) Six weeks after tdTomato-T4-2 cells were inoculated into NOD SCID mice (n = 4 mice) via intracardiac injection, overt brain metastases were excised, digested and sorted for tdTomato^{+} cells ("Macromet"). In parallel, the remainder of the brain was digested and sorted for tdTomato^{+} DTCs ("Micromet"). Samples were indexed, and then single cells underwent transcriptional profiling using the 10X Genomics Chromium platform. **c**) UMAP-based clustering revealed that tumour cells from Macromets and micromets segregate into

10 distinct clusters. **d**) Pie charts illustrate composition of micromets (*left*) and Macromets (*right*) by each cluster. Colors from UMAP plot in (**c**) apply to population distribution in (**d**). **e**) Genes that define clusters identified in (**c**) displayed as a heatmap according to normalized, mean expression. **f**) Pathway analysis of the top differentially expressed genes defining Cluster 0, Cluster 2, and Cluster 5 (dormant micrometastases) was conducted via the Kyoto Encyclopedia of Genes and Genomes (**KEGG**), and plotted by false discovery rate (**FDR**). **g**) Violin plots for "YAP target gene score" (*top*) and MKI67 expression (by log UMI; *bottom*) for each of the indicated clusters. * P=0.048 (YAP) and * P=8.08×10^{-83} (MKI67) comparing the conditions indicated by two-sided Wilcoxon rank sum test. **h**) Spearman correlation of YAP target gene score with indicated cell cycle scores. Associated P-values determined by two-tailed Spearman rank correlation.

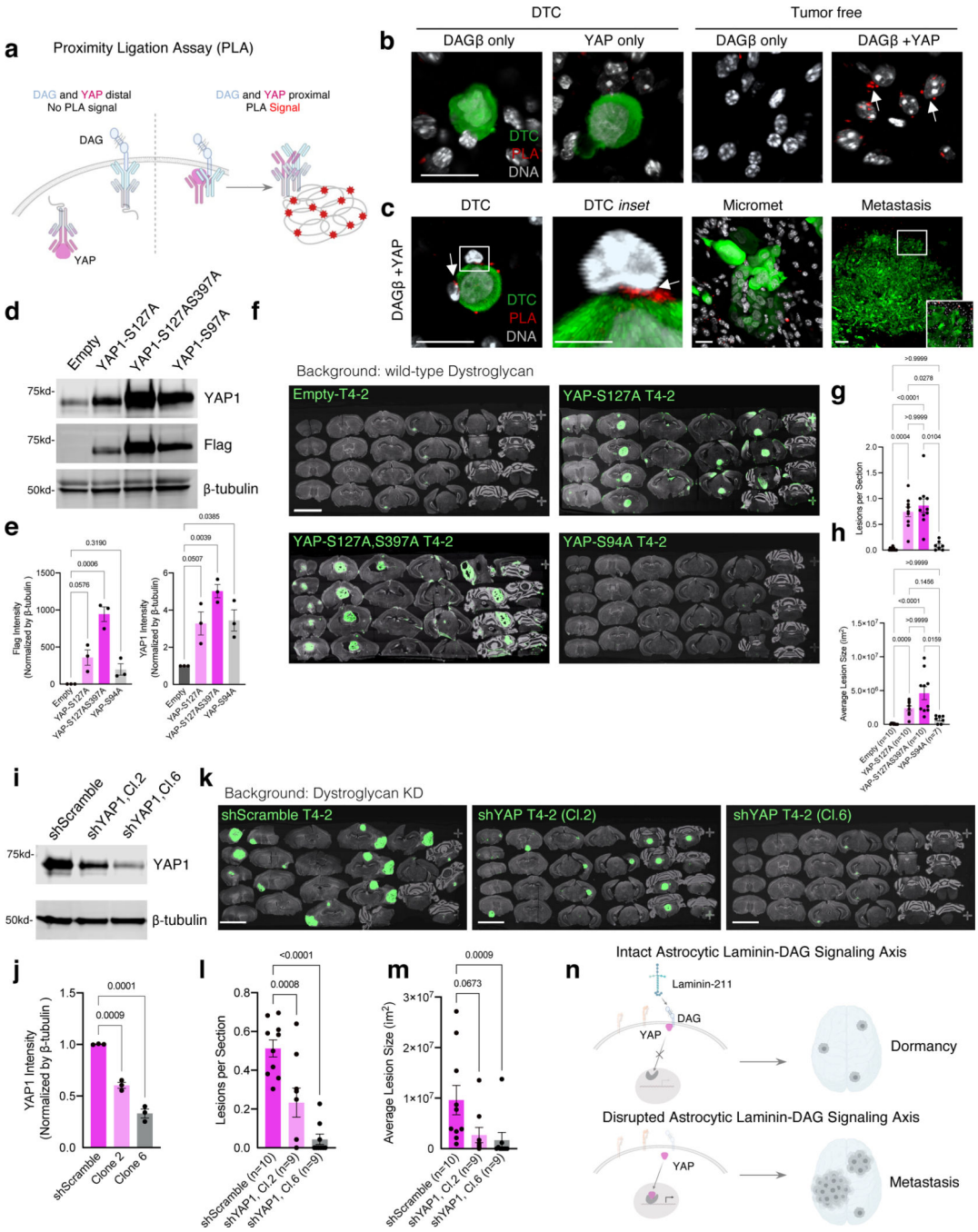

Figure 7: Dystroglycan physically associates with YAP, and may effect DTC quiescence by preventing YAP from shuttling to the nucleus.

a) Schematic of the proximity ligation assay (PLA) to detect DAG-YAP interaction. **b**) Control panels demonstrating the specificity of PLA signal (red spots). **c**) Positive PLA signal was observed along the plasma membrane of solitary DTCs (white arrows), but not in proliferative micrometastasis and macrometastasis. Scale bar = 20 μm for three leftmost panels, 100 μm for MACRO-Metastasis. **d**) Representative immunoblot of T4-2 cells transduced with control construct (Empty) or Flag-tagged YAP1-S127A, -S127A/

S397A or TEAD binding deficient -S94A mutants. Blot was co-stained for YAP1, Flag (M2), and β-tubulin as loading control. Blots representative of n=3 biologically independent experiments. **e**) Integrated intensity of Flag (M2) and YAP1 bands normalized to β-tubulin, and subsequently to the control Empty band on each blot quantified across n=3 biologically independent experiments. *P*-values were calculated by one-way ANOVA and Tukey's post hoc test. **f**) Representative immunostains of brain sections (20–25 sections/brain) from NOD-SCID mice, 6–8 weeks after intracardiac injection with eGFP-T4-2 cells transduced with the indicated YAP mutants: YAP-S127A (n=10 mice), YAP-S127A/S397A (n = 10 mice); and YAP-S94A, (n = 7 mice). Scale bar = 5 mm. Quantification of (**g**) metastatic lesions per section and (**h**) the average size of these lesions in these mice. *P*-values calculated by one-way ANOVA and Dunnett's multiple comparisons test. **i**) Representative immunoblot of T4-2-KD DAG (shDAG1, cl.4) cell line subsequently infected with non-targeting shRNA (shScramble) or one of two shRNA clones targeting human YAP1. Blot was co-stained for YAP1 and β-tubulin (loading control). **j**) Integrated intensity of YAP1 bands normalized to β-tubulin, then to shScramble band on each blot across n=3 biologically independent lysates. *P*-values calculated by one-way ANOVA and Tukey's post hoc test. **k**) Representative immunostains of brain sections (20–25 sections/brain) from NOD-SCID mice inoculated with eGFP-shDAG1-shScramble-T4-2 or eGFP-shDAG1-shYAP1-T4-2 cells, 6–8 weeks post-intracardiac injection (n = 9–10 mice per group). Scale bar = 5 mm. Quantification of (**l**) metastatic lesions per section and (**m**) the average size of these lesions in these mice. *P*-values calculated by one-way ANOVA and Dunnett's multiple comparisons test. **n**) Model of a brain-specific mechanism of DTC quiescence: astrocytic laminin-211 binds to DAG receptor on DTCs, sequestering YAP from the nucleus to drive quiescence. Disrupting laminin-211-DAG binding permits YAP nuclear shuttling, TEAD-dependent transcription, and metastatic colonization of brain. Data are presented as mean values +/− SEM.